J. Fluid Mech. (2020), *vol.* 888, A16. © The Author(s), 2020.
Published by Cambridge University Press
doi:10.1017/jfm.2019.1066

Hydrodynamic ejection caused by laser-induced optical breakdown

Jonathan M. Wang[1], **David A. Buchta**[2] **and Jonathan B. Freund**[1,3,†]

[1]Department of Mechanical Science and Engineering, University of Illinois at Urbana-Champaign, Urbana, IL 61801, USA

[2]The Center for Exascale Simulation of Plasma-coupled Combustion, University of Illinois at Urbana-Champaign, IL 61801, USA

[3]Department of Aerospace Engineering, University of Illinois at Urbana-Champaign, Urbana, IL 61801, USA

(Received 21 June 2019; revised 23 October 2019; accepted 18 December 2019)

A focused laser can cause local optical breakdown of a gas, which leads to rapid deposition of energy into a high-temperature plasma kernel that expands and induces a complex flow. For some conditions, hot gas is rapidly ejected along the laser axis up to distances several times the kernel size, with a particularly curious feature: relatively small changes in, for example, initial pressure can cause the direction of this ejection to reverse. Detailed axisymmetric simulations of a model energy kernel in an inert gas provide a hydrodynamic description of this phenomenon, reproducing key observations in corresponding experiments, including the vortex-ring-like features that constitute the ejection. These simulations are analysed to show how changes in the early-time kernel can lead to ejection or its reversal via alteration in the relative strength and position of the vorticity produced. A corresponding semi-infinite geometry is used to isolate two mechanisms: vorticity production by the generated shock and by baroclinic torque at the kernel boundary. Dependence on the initial kernel asymmetry is quantified, as it ultimately determines whether the vorticity, upon its subsequent evolution, develops into the ring-like structure that ejects. Even simple elongation of the energy kernel alone can reverse the direction.

Key words: compressible flows, vortex flows

1. Introduction

A focused laser pulse with sufficient energy causes optical breakdown of a gas and produces a high-temperature, high-pressure volume of ionized gas (Meyerand & Haught 1963). Even for a gas that is essentially transparent to the laser radiation, multi-photon ionization can produce free electrons that initiate a cascade process by which the gas becomes highly absorptive, leading to rapid heating (Morgan 1975; Harilal, Brumfield & Phillips 2015). By the end of the laser pulse, typically 10 ns in duration for the applications considered, the plasma kernel appears 1–3 mm long and 0.2–1 mm wide. It also appears to be axisymmetric about the laser axis, but is

---

[†] Email address for correspondence: jbfreund@illinois.edu

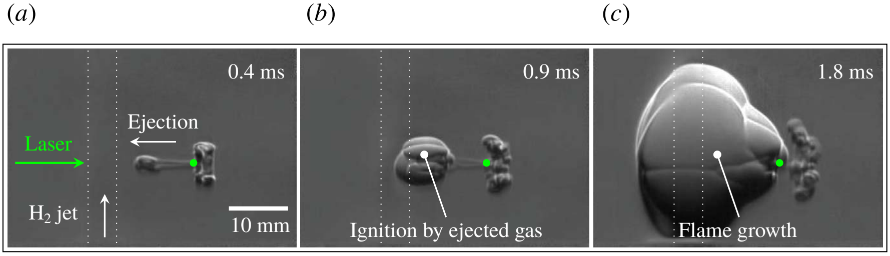

FIGURE 1. Laser-induced breakdown above a H_2, 4.8 mm-diameter jet into atmospheric-pressure air (Retter, Glumac & Elliott 2017). (*a*) The ejected hot gas (*b*) ignites the H_2/air mixture approximately 10 mm from the breakdown location, indicated by the green dot, leading to (*c*) flame growth.

often asymmetric in the direction of the laser (Adelgren *et al.* 2001; Glumac & Elliott 2007). The resulting expansion produces a shock wave that decouples from the kernel after approximately 1 μs, leaving behind a complex flow that mixes ambient gas with the hot kernel. In some cases, by approximately 100 μs, hot gas is ejected from the kernel along the laser axis, forming into an apparent vortex ring that can propagate beyond 10 mm from the breakdown location (figure 1*a*).

In a combustible mixture, the high temperature and presumably significant concentrations of radical species can ignite the gas and lead to a sustained flame. Such laser-seeded ignition is attractive because it deposits energy and radicals within a flow, away from material that might degrade, and with relatively precise control over timing and location (Ronney 1994; Phuoc 2006). Ignition in various flow configurations has been studied (Lacaze *et al.* 2009; Brieschenk, O'Byrne & Kleine 2013*a*; Massa & Freund 2017; Gibbons *et al.* 2018). Laser energy deposition has also been used in control for drag reduction (Riggins, Nelson & Johnson 1999) and controlling shock–shock interactions in supersonic flow (Kandala & Candler 2004; Adelgren *et al.* 2005).

Ignition by laser-induced breakdown (LIB) can be affected by a number of hydrodynamic and chemical processes. The ejection in particular, appearing as the so-called third lobe in combustible mixtures, can both enhance the rate of flame growth by increasing its surface area, yet also inhibit ignition by high strain rates (Schmieder 1981; Phuoc 2006). Supporting this, Dumitrache *et al.* (2017) observed enhanced flame growth after suppressing the ejection with a pre-ionization pulse, which was thought to reduce flame stretching. Similarly, Torikai, Soga & Ito (2017) showed that the ejection can extinguish a flame. In contrast, figure 1 shows that hot gas carried by the ejection can ignite gas some distance from the breakdown, which is potentially important in an inhomogeneous mixture with length scales comparable to the size of the ejection.

Even the qualitative character of the laser-induced ejection depends on local gas conditions. In multiple gases, Brieschenk, O'Byrne & Kleine (2013*b*) observed ejection towards the laser source at pressure $p = 1$ atm but away from the source at $p = 30$ atm. In subsequent work, a similar reversal in ejection direction was observed for relatively mild changes in pressure (0.59 to 1 atm), as shown in figure 2 (J. E. Retter and G. S. Elliott, personal communication 2017). Although precise measurements of the energy deposition are difficult to obtain, these early-time luminosity images suggest that the reversal coincides with changes in the shape

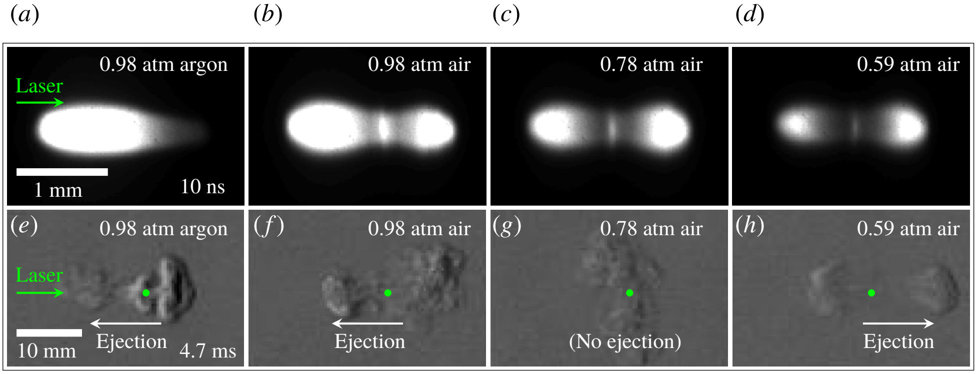

FIGURE 2. (*a–d*) Plasma luminosity in argon and air 10 ns after the laser pulse for a range of pressures. (*e–h*) Corresponding schlieren images 4.7 ms after the laser pulse showing ejection reversal (J. E. Retter and G. S. Elliott, personal communication). A 50 mJ, 532 nm single-mode laser with a focal length of 75 mm and pulse full-width-half-maximum of 7.7 ns was used. Emissions images were filtered with a central wavelength of 500 nm.

of kernel and that the underlying mechanism depends on the early-time energy distribution.

Other, similarly rapid and small energy depositions produce similar flows. For electrode discharges, a toroidal flow structure transports hot gas away from the breakdown region (Kono *et al.* 1988; Thiele, Warnatz & Maas 2000; Bane, Ziegler & Shepherd 2015). Kono *et al.* (1988) attributed this to low pressure in the spark gap caused by over-expansion of the plasma kernel, which induces an inward flow and production of vorticity that then propagates outward. In laser-induced breakdowns, low pressure produced by kernel over-expansion and an associated rarefaction wave were hypothesized to lead to a similar toroidal structure (Picone & Boris 1983; Spiglanin *et al.* 1995; Morsy & Chung 2002; Bradley *et al.* 2004). However, the specifics of how any low-pressure region leads to ejection or its reversal, especially its dependence on kernel shape (for example), remain unclear. Laser ablation of a solid surface produces a plume that ejects hot gas away from the target, which has also been attributed to over-expansion (Harilal *et al.* 2012). A different proposal is that the curved shock generated by the expanding plasma produces the vorticity (Svetsov *et al.* 1997), which was subsequently developed into a model for ejections from laser-induced breakdowns (Massa & Freund 2016). The relative contributions of the curved shock and overexpansion, however, have not been studied quantitatively. Furthermore, the connection between the early kernel geometry, vorticity generation and ultimate formation or reversal of the ejection remains unclear.

Although there are some apparent similarities with jetting by bubble collapse (e.g. Blake & Gibson 1987), the source of the driving pressure difference is fundamentally different. It has long been known that a collapsing bubble can become unstable (Plesset & Mitchell 1956), although it is unclear whether the gas-phase laser ejection, with its rapidly expanding hot plasma kernel and only weak subsequent contraction, can be described by similar mechanisms. We focus on mechanisms of vorticity generation. In the course of analysing the ensuing dynamics, we will draw qualitative analogies to the well-understood motion of uniform-density vortex rings (as in, for example, Picone & Boris (1988) and Ranjan *et al.* (2007)). Although density

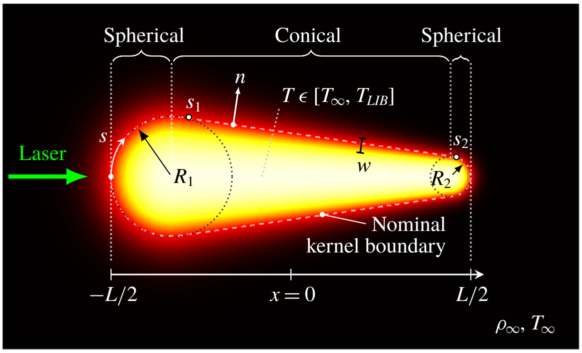

FIGURE 3. The model breakdown kernel consists of two spherical caps joined by a conical section. The contact boundary thickness $w \in [R_2, R_1]$ varies with s, and the temperature $T \in [T_\infty, T_{LIB}]$ varies with n.

variations persist locally, by the time this description becomes useful the flow speed is subsonic with weak compressibility effects. Incompressible vortex-ring theory is confirmed to predict the auto-advection speed of the ejected vorticity.

We focus on how the early kernel geometry leads to ejection and its reversal. The intense luminosity, rapid changes and small size of the plasma kernel make experimental diagnostics challenging, so we use well-resolved simulations of an idealized model breakdown (§ 2). While the breakdown physics is complex, a model geometry with basic front–rear asymmetry, coupled with an ideal-gas model, is confirmed to produce both ejection reversal and general agreement with vorticity measured with particle image velocimetry (PIV) (§ 3). To isolate vorticity production mechanisms, a corresponding semi-infinite geometry is introduced in § 4. These results are generalized to the finite-length geometry in § 5, where we analyse the effect of kernel asymmetry on vorticity generation. In § 6 it is shown how ejection and its reversal depend on the relative strength and position of ring-like vortical structures, which are ultimately determined by the kernel geometry.

2. Model configuration

2.1. *Kernel model*

The model is based on early-time ($t < 100$ ns) imaging of plasma kernels. The specific geometric details of the resulting kernel can depend on the pulse energy (Harilal *et al.* 2015), ambient pressure (Glumac & Elliott 2007), gas composition (figure 2) as well as the mode of laser operation, which can lead to multiple points of apparent plasma initiation and alter the plasma boundary growth (Nishihara *et al.* 2018). Simulations of the breakdown also show how the complex laser–plasma interaction can lead to the observed asymmetric structure (Kandala & Candler 2004; Alberti *et al.* 2019). In all these studies, the kernel is an approximately axisymmetric and elongated region with varying front–rear asymmetry. This consistent morphology motivates the model kernel introduced in figure 3: a high-temperature (T_{LIB}), high-pressure gas in a region constructed from two spherical caps joined by a conical section. The overall aspect ratio α and ratio of cap radii β are

$$\alpha \equiv \frac{L}{2R_1} \quad \text{and} \quad \beta \equiv \frac{R_1}{R_2}.$$

The breakdown is assumed to deposit zero momentum in the initially quiescent background ($\boldsymbol{u}=\boldsymbol{0}$) and to occur isochorically ($\rho=\rho_\infty$), ensuring mass conservation. The kernel temperature blends smoothly with the ambient over local length scale w, which varies along the tangential coordinate s as

$$w(s)=\begin{cases} R_1, & s<s_1,\\ \dfrac{s-s_2}{s_1-s_2}R_1+\dfrac{s-s_1}{s_2-s_1}R_2; & s_1\leqslant s\leqslant s_2,\\ R_2, & s_2<s, \end{cases}$$

where s_1 and s_2 are set so the spherical sections are tangent to the conical section. The temperature

$$T(n)=T_\infty+(T_{LIB}-T_\infty)f(n) \tag{2.1}$$

varies with the normal coordinate n, where $f(n)\equiv\frac{1}{2}[1-\tanh(\sigma n)]$ and σ is set so $f(w/2)=0.1$ and $f(-w/2)=0.9$.

2.2. *Governing equations*

The flow equations are formulated for an ideal gas in axisymmetric cylindrical coordinates for the conserved flow variables $\boldsymbol{Q}=\{\rho,\ \rho u_x,\ \rho u_r,\ \rho e\}$, where ρ is the density, and u_x and u_r are the velocity components. The total energy e and internal energy e_{int} are

$$e\equiv e_{int}+\frac{1}{2}|\boldsymbol{u}|^2 \quad \text{and} \quad e_{int}=\frac{1}{\gamma-1}\frac{p}{\rho}=\frac{1}{\gamma}c_pT,$$

where $\gamma=1.4$ is the ratio of specific heats and c_p the specific heat at constant pressure. Unless otherwise noted, $T_{LIB}=26.9T_\infty$ and the Reynolds number $Re_L\equiv\rho_\infty a_\infty L/\mu=4.4\times10^4$ would correspond to a kernel length of $L=2$ mm in air at $p_\infty=1$ atm and $T_\infty=298$ K, where $\mu=1.8\times10^{-5}$ Pa s is the dynamic viscosity and a_∞ is the ambient speed of sound. For a strong ejection with speed $U=70\ \text{m s}^{-1}$ based on experimental imaging, a flow-velocity Reynolds number is $Re_U\equiv\rho_\infty UL/\mu\approx9200$. Although at early times $\gamma=5/3$ would better represent the dissociated gas, a simulation with this γ evolves similarly, with net circulation differing by less than 6 % for the case considered in § 3.2. The bulk viscosity $\mu_B=0.6\mu$ is chosen as a model for air (Thompson 1971). The Prandtl number $Pr\equiv c_p\mu/\lambda=0.72$ is also taken to be that of air, where λ is the thermal conductivity. The viscosity, specific heat, and thermal conductivity are assumed to be constant, which is clearly an approximation, especially in the hot plasma core. This perfect gas model is used to represent the range of possible phenomenologies and elucidate underlying hydrodynamic mechanisms rather than provide full quantitative detail at these extreme conditions. Previous work (Ghosh & Mahesh 2008) suggests that additional physics such as chemistry or temperature-dependent transport properties would not significantly alter the flow pattern. Moreover, we show that the principal vorticity-generating mechanisms occur outside the hottest regions of the kernel. Our reduced model will be shown to reproduce key experimental observations in § 3.1, and viscous effects are assessed in more detail in § 4.5.

Of the six non-dimensional parameters α, β, T_{LIB}/T_∞, Re_L, Pr and γ, dependence on the geometry parameters α and β is our primary concern. Dependence on $Re_{R_2}\equiv\rho_\infty a_\infty R_2/\mu$ will be considered in § 5.

	Type	Mesh spacing	Extents	Size	Simulated time
1	Uniform	$5\times 10^{-4}L$	$3.06L\times 1.25L$	6120×2500	$ta_\infty/L\lesssim 0.5$
2	Uniform	$1\times 10^{-3}L$	$6.12L\times 2.5L$	6120×2500	$0.5\lesssim ta_\infty/L\lesssim 2.0$
3	Stretched	$3\times 10^{-3}L$	$40L\times 20L$	7380×3690	$ta_\infty/L\gtrsim 2.0$

TABLE 1. Three simulations on successively coarser meshes are used to compute each LIB solution. For the stretched mesh, the mesh spacing corresponds to $\Delta x_{min}=\Delta r_{min}$. The simulated times depend on the when the shock reaches the boundaries of meshes 1 and 2 and vary across cases.

A passive scalar ξ is used to track the evolving kernel, especially its boundary as labelled in figure 3. It is initialized with the signed distance $\xi(t=0)=n$ from the $n=0$ boundary and subsequently advects,

$$\frac{\partial(\rho\xi)}{\partial t}+\nabla\cdot(\rho\xi\boldsymbol{u})=0. \tag{2.2}$$

The nominal contact boundary is thus

$$\mathrm{CB}\equiv\{(x,r)\mid\xi(x,r)=0\}. \tag{2.3}$$

2.3. *Simulation method*

To discretize the governing equations, eighth-order, nine-point centred finite-difference stencils for first and second derivatives are used in concert with an explicit eighth-order, nine-point filter (Lele 1992) applied at each time step. The shocks generated are relatively weak and modelled in the Navier–Stokes limit, with confirmed mesh independence. A shock-capturing scheme was not used due to concerns regarding the accuracy of vorticity generation by shock–shock or shock–vorticity interactions. Although standard schemes are designed and tested to produce accurate pressure and density fields (Bogey, De Cacqueray & Bailly 2009; Lo, Blaisdell & Lyrintzis 2010), shear and vorticity generation is less often assessed. Studies with weighted essentially non-oscillatory schemes (WENO) suggest that it may not be suitable for the present analysis of vorticity production (Pirozzoli 2002; Johnsen *et al.* 2010).

The governing equations at the $r=0$ coordinate singularity are evaluated in the $r\rightarrow 0$ limit, with

$$u_r=0,\quad \frac{\partial\rho}{\partial r}=0,\quad \frac{\partial p}{\partial r}=0,\quad \frac{\partial u_x}{\partial r}=0\quad\text{and}\quad \frac{\partial^2 u_r}{\partial r^2}=0 \tag{2.4a–e}$$

based on continuity and differentiability at $r=0$ (e.g. Liu & Wang 2009). The same interior stencils are also used at $r=0$, although they are constrained to enforce (2.4) using the fact that ρ, u_x and e are even functions of r and that u_r is an odd function of r. Thus eighth-order spatial accuracy is achieved everywhere in the flow except the outer boundaries.

Because the kernel expands and gradients weaken in time, less spatial resolution is required at later stages. To reduce computational cost, the solution is computed using the three successively coarser meshes described in table 1 and figure 4. Before the shock reaches the mesh boundary, the solution is interpolated onto the next mesh with

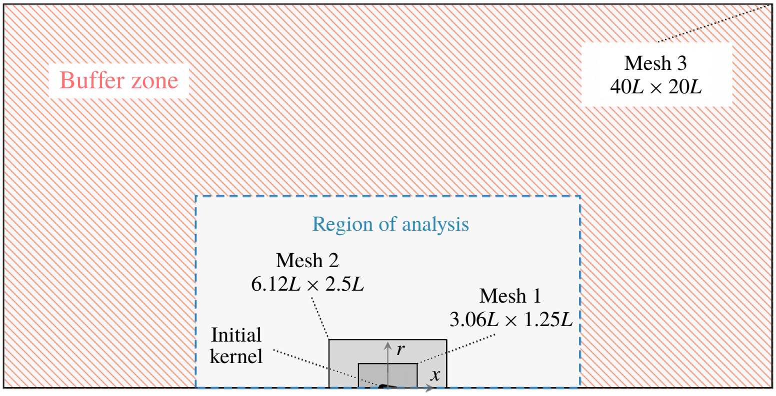

FIGURE 4. Diagram showing the relative size of each mesh in table 1.

fourth-order bicubic polynomial splines. The first two meshes are uniform. The third mesh is stretched, with coordinates mapped independently from $z_{1,2} \in [0, 1]$ to (x, r) using

$$x = \frac{40L}{g}\left\{\frac{a}{2b}[\log(\cosh[b(z_1-1)]) - \log(\cosh[bz_1]) - \log(\cosh b)] + (1+a)z_1\right\} - 20L,$$

$$r = \frac{40L}{g}\left\{\frac{a}{2b}\left[\log\left(\cosh\left[b\frac{z_2-1}{2}\right]\right) - \log\left(\cosh\left[b\frac{z_2+1}{2}\right]\right) - \log(\cosh b)\right] + (1+a)\frac{z_2+1}{2}\right\} - 20L,$$

where

$$g \equiv 1 + a - \frac{a}{b}\log(\cosh b),$$

and $a = 112$ and $b = 96.2$ are chosen so that mesh spacing in the region $x \in [-10L, 10L]$, $r \in [0, 10L]$ is effectively uniform, with Δx and Δr within 1 % of $\Delta x_{min} = \Delta r_{min} = 0.003L$. All reported simulation results on this mesh are from this nearly uniform region. For most of the results the meshes in table 1 are used. Doubling the density of these meshes results in less than 1 % change in the net circulation and maximum flow velocity at $T_{LIB} = 26.9T_\infty$. For the most intense cases in § 4.4, greater resolution ($1.25 \times 10^{-4}L$) was required for this degree of mesh independence; for those conditions it was further verified that the post-shock pressure and velocity agree with the one-dimensional equivalent Riemann problem to within 0.4 %. To further assess accuracy, particularly for analysis of shock-generated vorticity, a still finer spacing is used ($2.5 \times 10^{-5}L$), which confirmed insensitivity to the mesh.

At the outer boundary of the third mesh, the pressure p_∞ is imposed using the characteristic formulation of Thompson (1990) in conjunction with the stabilization procedure of Poinsot & Lele (1992). In addition, a buffer zone (Freund 1997; Colonius 2004), with a source term added to the flow equations $\boldsymbol{Q}_t + \mathcal{N}(\boldsymbol{Q}) = \boldsymbol{0}$, is used with support near the boundary,

$$\boldsymbol{Q}_t + \mathcal{N}(\boldsymbol{Q}) = \max(\sigma_x, \sigma_r)(\boldsymbol{Q}_\infty - \boldsymbol{Q}), \tag{2.5}$$

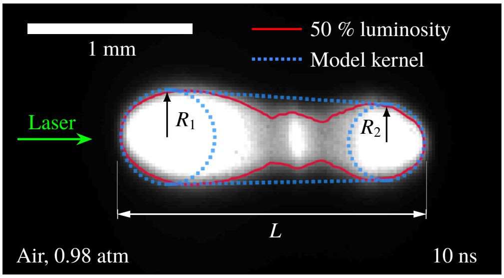

FIGURE 5. The model kernel is fit to the 50 % normalized luminosity level of the early-time kernel image, reproduced here from figure 2(*b*). R_1 and R_2 are chosen as the maximum radial extents of the left and right halves, respectively, with their centres chosen such that the model kernel matches in length.

where

$$\sigma_x = \begin{cases} \left(\dfrac{|x|}{10L} - 1\right)^2, & x > 10L \text{ or } x < -10L \\ 0, & \text{otherwise} \end{cases} \qquad \sigma_r = \begin{cases} \left(\dfrac{r}{10L} - 1\right)^2, & r > 10L \\ 0, & \text{otherwise} \end{cases}$$

and $\boldsymbol{Q}_\infty \equiv \{\rho_\infty, 0, 0, \rho_\infty e_\infty\}$. All simulations are advanced with an explicit fourth-order Runge–Kutta scheme using a time step

$$\Delta t = \min_{\{mesh\}} \frac{\text{CFL}}{\dfrac{|u_x| + a}{\Delta x} + \dfrac{|u_r| + a}{\Delta r}},$$

where a is the local speed of sound and $\text{CFL} = 0.8$.

3. Ejection phenomenology

3.1. *Comparison with experiment*

We first confirm that the model reproduces key experimental observations. For this, the model parameters α, β, and L are based on early-time imaging – figure 5 shows the fitting process – and T_{LIB} is chosen such that the energy deposited matches measurement. Given the assumptions (idealized geometry, uniform and instantaneous energy deposition, ideal-gas properties), we have no expectation of precise agreement. Still, figure 6 shows that the vorticity agrees qualitatively with measurement: the predominantly $\omega_\theta < 0$ vorticity is ejected leftward, whereas the predominantly $\omega_\theta > 0$ vorticity is located farther from the axis and, in this case, moves slowly rightward. There is quantitative agreement in net circulation until at least 200 µs, consistent with the similar auto-advection speeds of the ejection. By 500 µs the on-average axisymmetry is apparently disrupted by shot-to-shot variation. Onset of three-dimensional instabilities will affect this late-time development, though the degree of comparison here suggests that it does not alter the mechanisms of vorticity production leading to the organized motion, which will be shown to occur well before the times of figure 6. The relative temperature distribution in figure 7 shows similar agreement with different measurements (Glumac, Elliott & Boguszko 2005): the ambient gas breaches the kernel at approximately 50 µs, and the hottest gas is pushed outward from the symmetry axis.

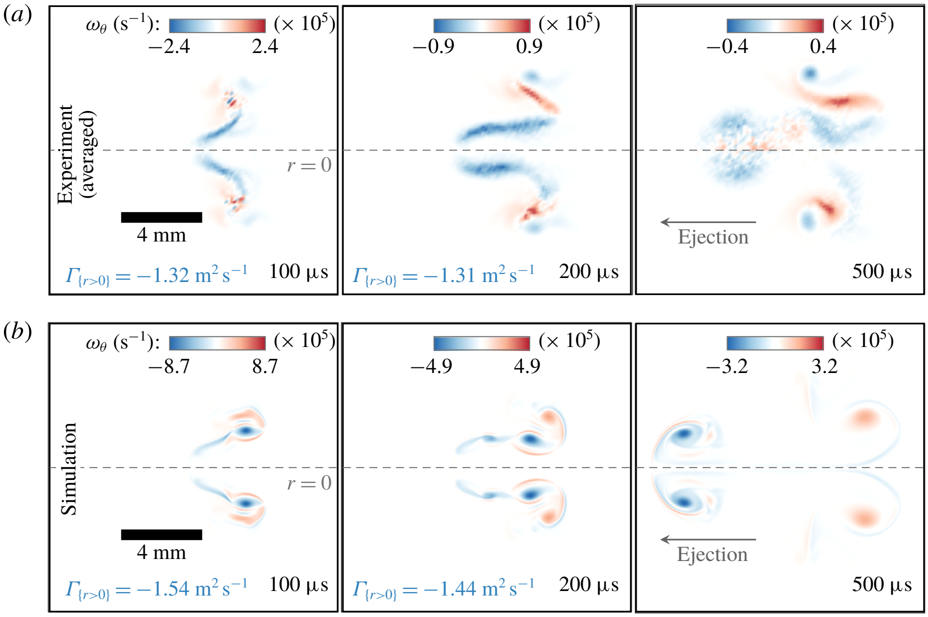

FIGURE 6. (*a*) PIV-measured azimuthal vorticity averaged over 100 breakdowns in 1 atm air (Koll, Elliott & Freund 2020), with the same laser configuration as in figure 2. (*b*) Simulation with the present model using $\alpha = 3.23$, $\beta = 1.24$ and $L = 1.84$ mm based on figure 5. Although simulation of an individual breakdown leads to sharper features than the averaged experimental data (note the different colour levels), the net circulation $\Gamma \equiv \iint \omega_\theta \, \mathrm{d}x \, \mathrm{d}r$ in the $r > 0$ half-plane matches to within 10 % at 200 µs, with $\Gamma_{\{r>0\}}$ and $\Gamma_{\{r<0\}}$ differing by less than 1 % in the experiment.

3.2. *Kernel evolution and ejection*

A case with $\alpha = 3$ and $\beta = 3$ is described here in detail. The geometric parameters are based on general observations of luminous regions in experiments, and a full range is considered subsequently. Figure 8 shows the kernel volume, based on the nominal contact boundary (2.3), and its mean interior pressure and temperature, defined as

$$\overline{p} \equiv \frac{\gamma - 1}{\gamma} c_p \overline{\rho}\,\overline{T} \quad \text{and} \quad \overline{T} \equiv \frac{\gamma}{c_p} \overline{e}_{int}, \tag{3.1}$$

where

$$\overline{\rho} \equiv \frac{1}{V_\Omega} \int_\Omega \rho \, \mathrm{d}V \quad \text{and} \quad \overline{e}_{int} \equiv \frac{1}{\overline{\rho} V_\Omega} \int_\Omega \rho e_{int} \, \mathrm{d}V,$$

with Ω the region enclosed by the contact boundary (2.3) and V_Ω its volume. Both $\overline{T}$ and $\overline{p}$ decrease rapidly as the kernel expands, producing the shock wave visualized in figure 9(*a*). The part of this shock emanating from the conical section of the model geometry, approximately normal to the axis, is strongest, which is consistent with experimental observations (Gregorčič, Diaci & Možina 2013). The kernel reaches its maximum volume at $t \approx 0.5L/a_\infty$, at which point the interior pressure has dropped below p_∞ and subsequently begins to equilibrate.

This early dynamics induces the complex flow shown in figure 9(*b*), which marks the beginning of the ejection. A region of negative-x momentum near $r = 0$ on the

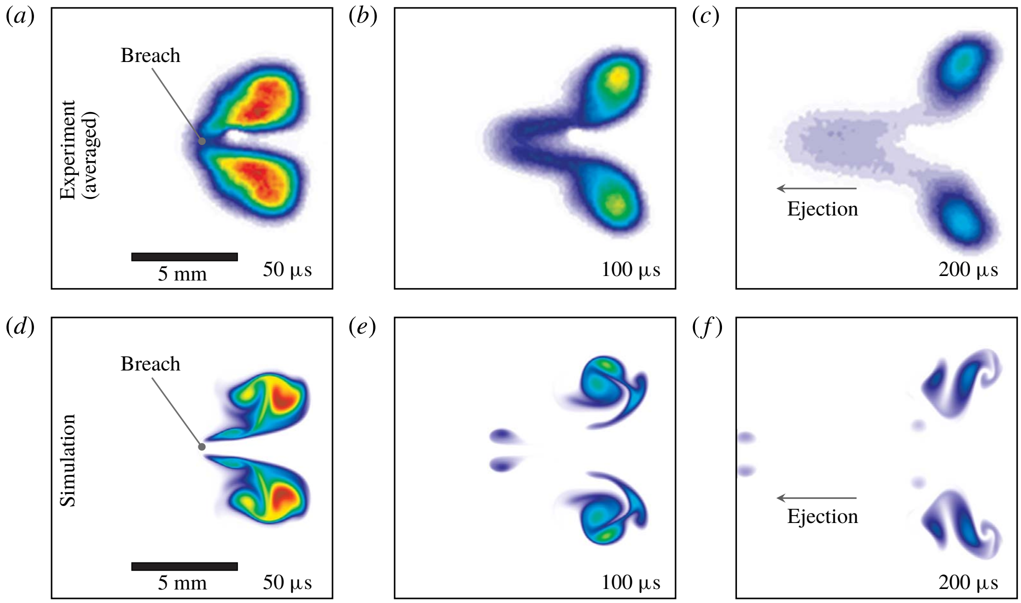

FIGURE 7. (*a–c*) Temperature averaged over 200 breakdowns in 0.97 atm air (Glumac *et al.* 2005), adapted here with permission. (*d–f*) Simulation with the present model using $\alpha = 3.24$, $\beta = 1.92$ and $L = 2.71$ mm based on plasma kernel imaging at 25 ns in the corresponding experiments. A direct comparison of temperature values is not informative for the perfect gas model of the present simulations.

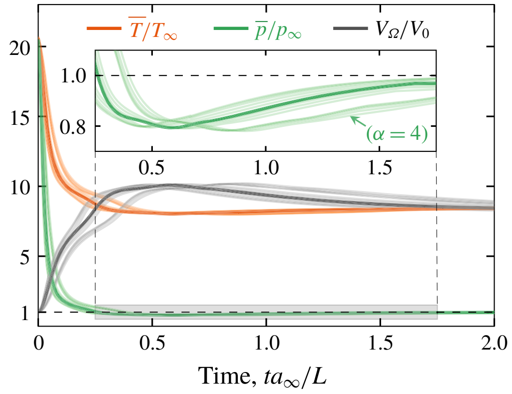

FIGURE 8. Relative mean pressure and temperature (3.1) and kernel volume, with V_0 the initial volume. Fainter lines show only mild variation due to geometry ($\alpha \in [2, 4]$, $\beta \in [1.2, 3.0]$) relative to the $\alpha = 3$, $\beta = 3$ baseline case; $\alpha = 4$ kernels attain $\min \overline{p}$ and $\max V_\Omega$ later in time.

right side of the kernel is associated with negative vorticity, which can be interpreted as auto-advecting leftward. Most of this momentum is in the dense inward-flowing ambient gas outside the kernel boundary. It breaches the hot, low-density ($\rho \approx \rho_\infty/8$) kernel at $t \approx 9.0L/a_\infty$, as shown in figure 9(*c*).

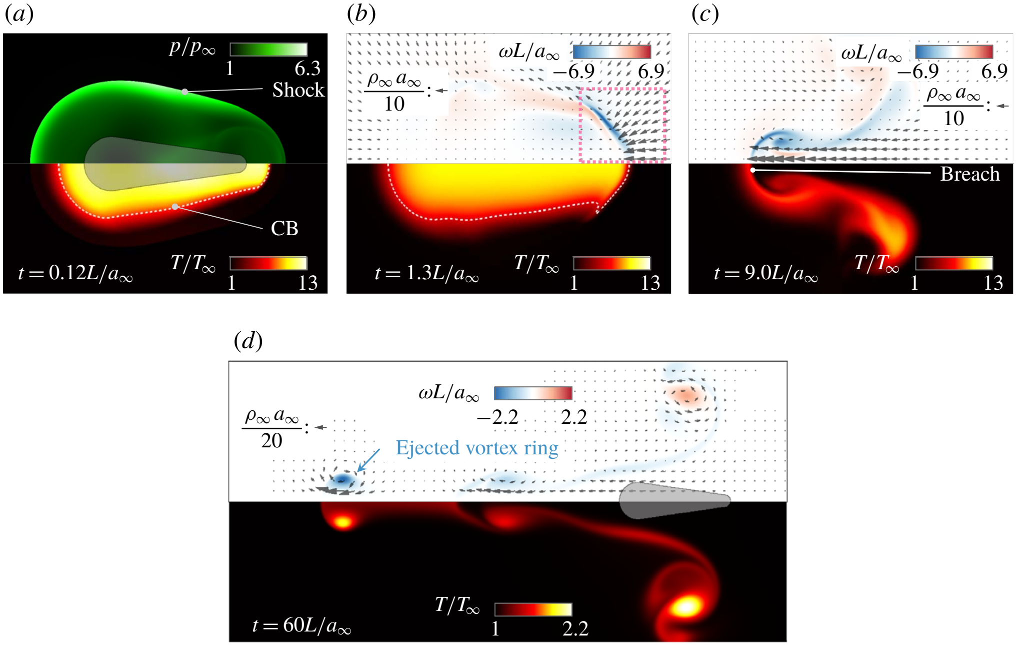

FIGURE 9. Formation of a leftward ejection with $\alpha = 3$ and $\beta = 3$. (*a*) The shock, visualized with the pressure, propagates outwards from the contact boundary (CB); the initial kernel is shown in grey. (*b–d*) The vorticity distribution, $\rho\boldsymbol{u}$ vectors, and ejection as labelled. The dotted box in (*b*) highlights the region of negative x-momentum leading to the ejection. Momentum instead of velocity vectors are shown due to the density variation.

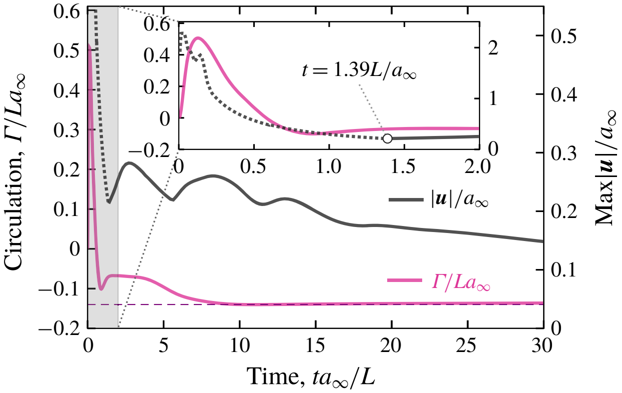

FIGURE 10. Circulation and maximum speed. The dashed line at $\Gamma = -0.14La_\infty$ is shown for reference. Before $t=1.39L/a_\infty$, max $|\boldsymbol{u}|$ is associated with the shock and marked by a dotted line.

Figure 10 shows the circulation

$$\Gamma \equiv \iint \omega \, \mathrm{d}r \, \mathrm{d}x, \tag{3.2}$$

where

$$\omega \equiv \omega_\theta = \frac{\partial u_r}{\partial x} - \frac{\partial u_x}{\partial r}.$$

Rapid production of circulation occurs before $t = 2L/a_\infty$, which coincides with the changes in pressure seen in figure 8. Beyond this time the flow is subsonic and qualitatively consistent with auto-advection of existing vorticity, albeit in a variable-density fluid. This is not expected to be significant in interpreting the evolution since 79 % of the volume within L of the kernel centre has $\rho > 0.8\rho_\infty$. After the kernel is breached at $t \approx 9L/a_\infty$ (figure 9*c*), the circulation remains approximately constant, and the negative vorticity separates from the nominal breakdown location and propagates as a hot vortex ring (figure 9*d*). By $t = 60L/a_\infty$ its speed is within 20 % of the standard auto-advection speed U of an incompressible and constant-density vortex ring,

$$U = \frac{\Gamma_0}{4\pi r_0}\left[\ln\left(\frac{8r_0}{a}\right) - \frac{1}{4}\right]. \tag{3.3}$$

For making this estimate, its nominal position (x_0, r_0) is marked by the peak vorticity ω_0, the circulation Γ_0 is the total within $x \in [x_0 - 2r_0, x_0 + 2r_0]$ (as in Archer, Thomas & Coleman (2008)), and the radius $a = \sqrt{\Gamma_0/\pi\omega_0}$ is such that a uniform vortex core with $\omega = \omega_0$ would have the same circulation. The specific sources of vorticity will be analysed in detail in §§ 4 and 5.

3.3. *Dependence on kernel geometry*

The hydrodynamic development depends on the initial kernel geometry, which we vary over $\alpha \in [2, 12]$ and $\beta \in [1/3, 3]$ to include a range of observations (Glumac & Elliott 2007; J. E. Retter and G. S. Elliott, personal communication 2017). Figure 11 shows that the net circulation Γ changes sign with both α and β, with corresponding reversals in the ejection, quantified by its length L_E. Fore–aft symmetry effects ($\beta \lessgtr 1$), which appear to correspond to early-time luminosity imaging (figure 2*b*–*d*), can obviously lead to reversal, with more asymmetric kernels (larger β or $1/\beta$) producing greater circulation and a more pronounced ejection. Closer inspection also suggests that the ejected vortex ring of such kernels has a smaller radius and propagates faster (e.g. $\beta = 1.5$ versus $\beta = 3$), consistent with (3.3). For near-symmetric kernels ($1/1.2 \lesssim \beta \lesssim 1.2$) a distinct ejection is not observed, and the vorticity instead collects into a ring pair that travels outward from the symmetry axis. More curiously, increasing the aspect ratio beyond $\alpha \approx 5$ also leads to reversal, though the rightward ejection is somewhat weaker than its leftward counterpart. Details of the ejection failure at $\beta \approx 1.2$ and the reversal at $\alpha \approx 5$ will be discussed in § 6.

4. Mechanisms of vorticity generation: a semi-infinite analogue

4.1. *Configuration*

An analogous, semi-infinite geometry (figure 12) is introduced here to isolate vorticity-generating mechanisms from subsequent vortex formation and interaction dynamics, which are considered in more detail subsequently. The thermal initial condition (2.1) is used for a cylindrical section that extends effectively to $x \to -\infty$ and capped by a hemisphere at $x = 0$. Practically, this configuration was implemented in a sufficiently long domain to preclude interactions between the ends for the times considered. Without a length scale analogous to L, we use $Re_{R_2} \equiv \rho_\infty a_\infty R_2/\mu = 2400$

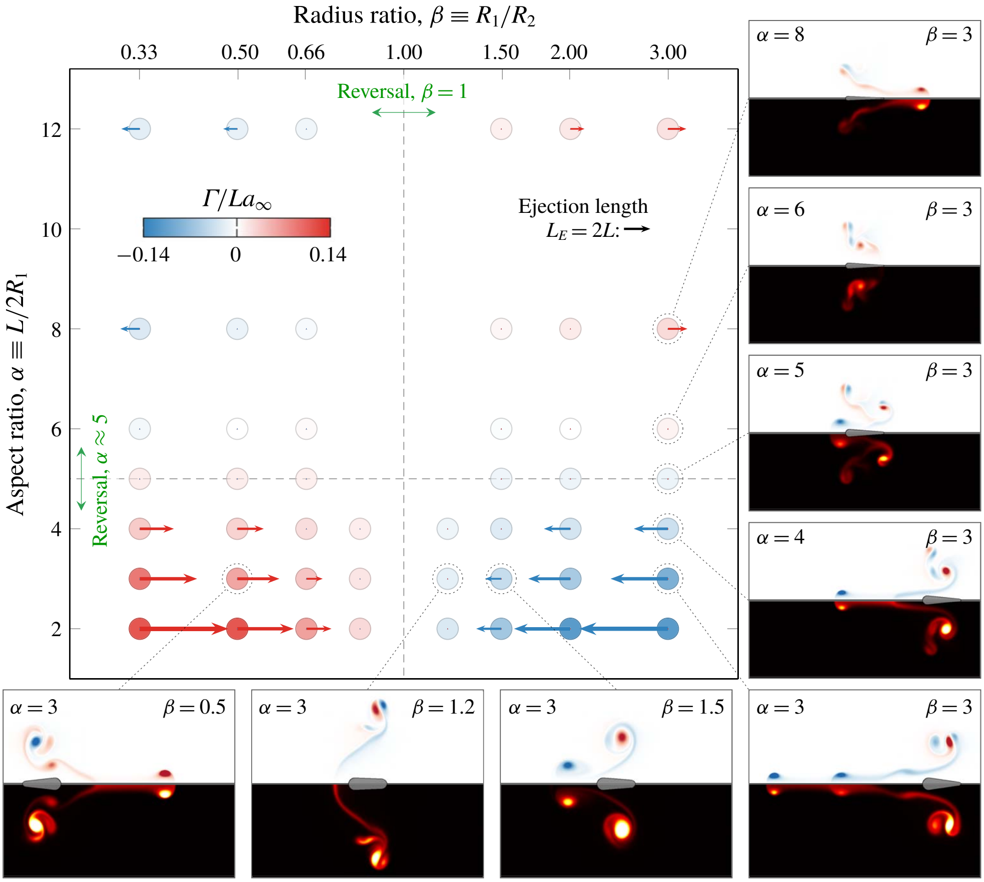

FIGURE 11. Dependence of the ejection character on α and β, visualized with the vorticity and temperature at $t = 100L/a_\infty$, with the initial kernel in grey. Each data point is coloured by the net circulation Γ (3.2), and arrows correspond to the ejection length L_E, taken to be the axial distance from the centre of the initial kernel to the point of peak vorticity $\max|\omega|$. Only $L_E > L$ arrows are shown to indicate cases in which a clear ejection is observed.

to be consistent with the baseline $\alpha = 3$, $\beta = 3$ geometry for which $L = 18R_2$. This configuration has four non-dimensional parameters (Re_{R_2}, T_{LIB}/T_∞, γ, Pr), which is simplifying since it avoids the α and β parameters of § 3.3. Dependence on Re_{R_2} is quantified in § 4.5.

The flow generated by this configuration is shown in figure 13. As for the finite-L cases, the expanding kernel produces a shock, behind which there is transient subambient pressure near the kernel (figure 13*a*). By $t = 40R_2/a_\infty$ (figure 13*b*), obvious negative vorticity has been produced near the end, and by $t = 236R_2/a_\infty$ the associated negative-x flow at the end of the kernel has penetrated into the low-density kernel (figure 13*c*). The evolution after this point is phenomenologically consistent with auto-advection of the vorticity, with a maximum velocity less than $0.1a_\infty$. The faster vorticity advection near the axis resembles that of the finite-length cases (figure 9*c*).

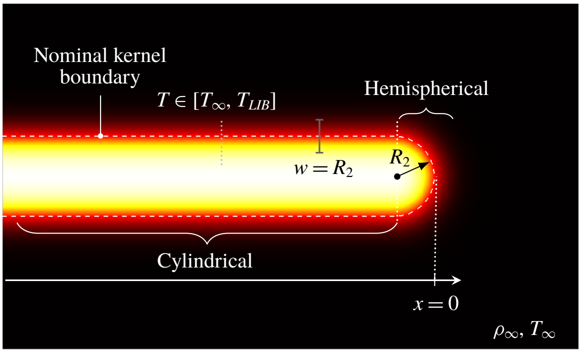

FIGURE 12. The semi-infinite geometry consists of an infinitely long cylindrical section and a hemispherical cap.

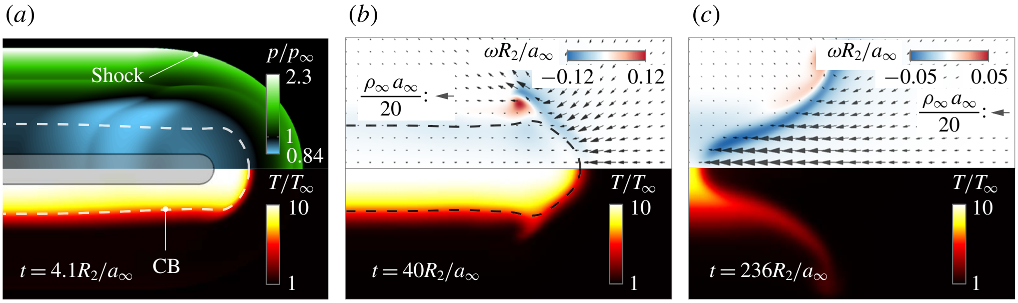

FIGURE 13. (*a*) The shock decouples from the kernel, initially in the grey region, and (*b*) leaves behind a region of negative vorticity that (*c*) penetrates into the hot, low-density kernel. Vectors correspond to $\rho \boldsymbol{u}$.

4.2. *Vorticity generation by the shock*

By $t = 1.19R_2/a_\infty$, the kernel has cooled from $26.9T_\infty$ initially to a peak of $13.0T_\infty$, and the shock has decoupled from the hot gas, as shown in figure 14(*a*), leaving a triangle-like region of negative vorticity behind it. Positive vorticity is also produced along the contact boundary during this early expansion, though this is largely cancelled by a subsequent mechanism, which will be discussed in § 4.3.

The dominant source of the negative vorticity is tangential variation in the shock strength, quantified by the pressure immediately behind the shock (figure 15). Away from the cylindrical–spherical junction, it matches the pressure at these short times for corresponding spherical and cylindrical cases. It is the faster decay of the spherical shock that leads to the pressure gradient between the two regions.

Theoretical estimates for shock-generated vorticity were independently derived by Truesdell (1952) and Lighthill (1957) and generalized by Hayes (1957). For an unsteady, axisymmetric shock of varying strength,

$$\omega = \frac{\rho_s}{\rho_\infty}\left(1 - \frac{\rho_\infty}{\rho_s}\right)^2 \frac{\partial U}{\partial s},$$

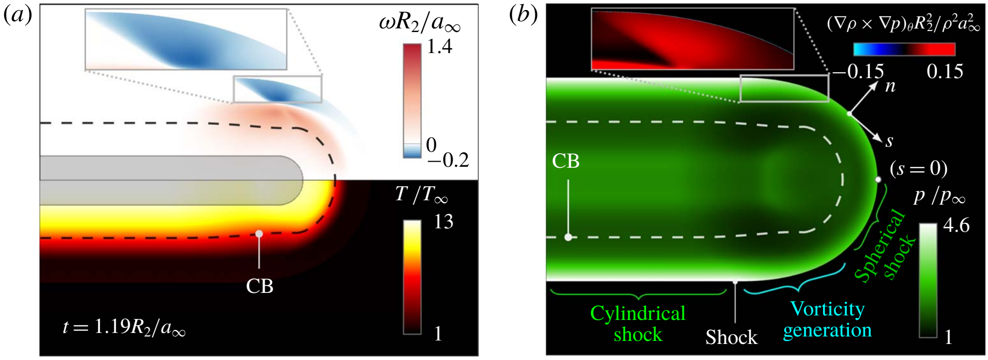

FIGURE 14. (*a*) Negative vorticity generation by the shock at $t = 1.19R_2/a_\infty$ is (*b*) partially cancelled by positive baroclinic torque. The initial kernel is shaded grey in (*a*).

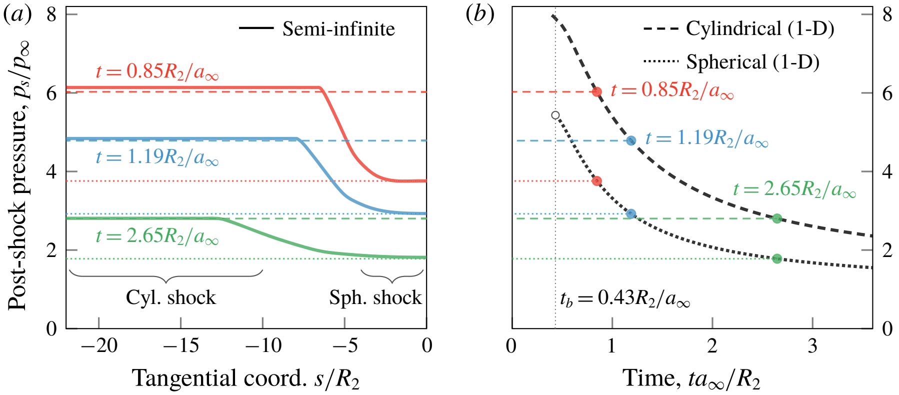

FIGURE 15. Pressure behind the shock for the (*a*) axisymmetric semi-infinite kernel and (*b*) corresponding spherically and cylindrically symmetric cases. 1-D, one-dimensional; Cyl., cylindrical; Sph., spherical.

where ρ_s is the density behind the shock, U is the shock speed and s is the local tangent coordinate. Applying shock-jump relations yields

$$\omega = \frac{\gamma+1}{4\gamma}\frac{\rho_s}{\rho_\infty}\left(1-\frac{\rho_\infty}{\rho_s}\right)^2 \frac{1}{\sqrt{\dfrac{\gamma-1}{2\gamma}+\dfrac{\gamma+1}{2\gamma}\dfrac{p_s}{p_\infty}}}\frac{a_\infty}{p_\infty}\frac{\mathrm{d}p_s}{\mathrm{d}s}, \tag{4.1}$$

where p_s is the pressure behind the shock. Thus, the region of negative vorticity in figure 14 is produced by the tangential pressure gradient in figure 15(*a*) and grows in size as this region grows along the shock front.

In figure 14(*b*), it is also evident that a distributed baroclinic torque behind the shock acts to cancel the shock-generated vorticity. The misalignment of $\nabla\rho$ and ∇p that drives this is illustrated schematically in figure 16(*a*). In the effectively spherical and cylindrical regions, pressure and density closely match the corresponding one-dimensional case and therefore have parallel gradients. Between these regions, the higher pressure behind the cylindrical shock (figure 16*b*) leads to misalignment.

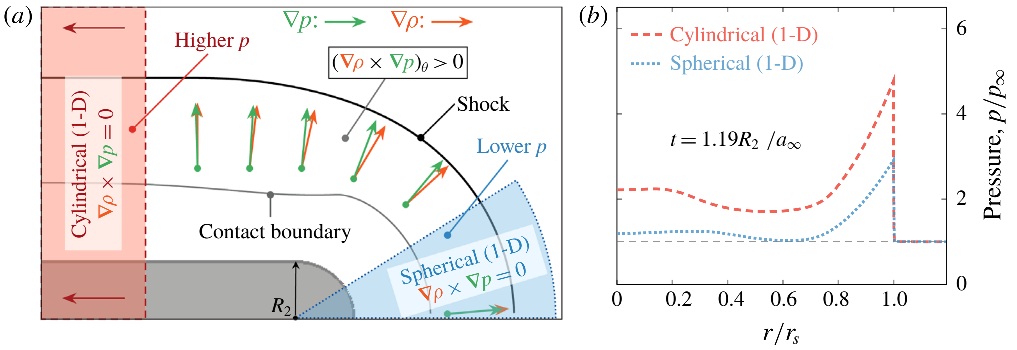

FIGURE 16. (*a*) Schematic showing the post-shock misalignment of $\nabla\rho$ and ∇p between the effectively one-dimensional regions, and (*b*) corresponding pressure profiles, where r_s is the position of the shock.

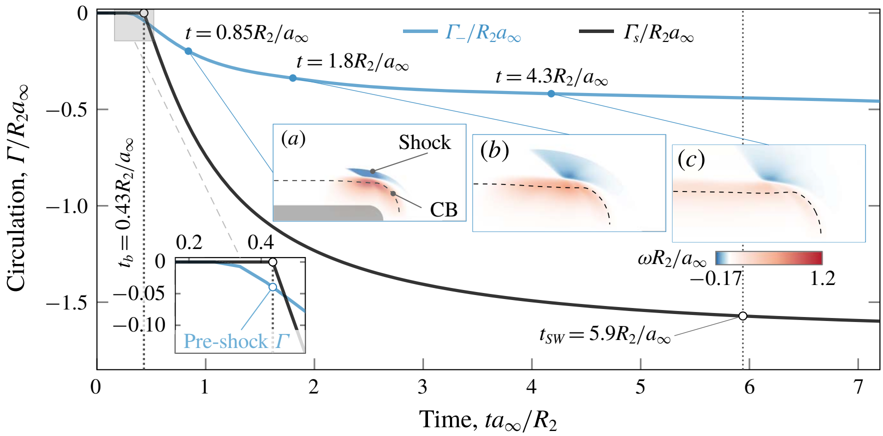

FIGURE 17. Total negative circulation Γ_- (4.2) and shock-generated circulation Γ_s (4.3).

The net effect of these two vorticity sources – negative at the shock and positive behind the shock – is quantified by the negative circulation Γ_-,

$$\Gamma_-(t) \equiv \iint_{\omega<0} \omega(t)\,\mathrm{d}x\,\mathrm{d}r, \tag{4.2}$$

shown in figure 17, which decreases monotonically as the shock propagates. Their respective contributions can be estimated by integrating (4.1) for the shock-generated circulation,

$$\Gamma_s(t) \equiv \iint \omega(t)\,\mathrm{d}n\,\mathrm{d}s,$$

using the shock speed for $\mathrm{d}n = U\,\mathrm{d}t$, which upon applying the shock-jump relation as in (4.1) yields

$$\Gamma_s(t) = \frac{\gamma+1}{4\gamma}\int_{\tau=t_b}^{t}\int_{-\infty}^{0}\frac{\rho_s}{\rho_\infty}\left(1-\frac{\rho_\infty}{\rho_s}\right)^2\frac{a_\infty^2}{p_\infty}\frac{\mathrm{d}p_s}{\mathrm{d}s}\,\mathrm{d}s\,\mathrm{d}\tau.$$

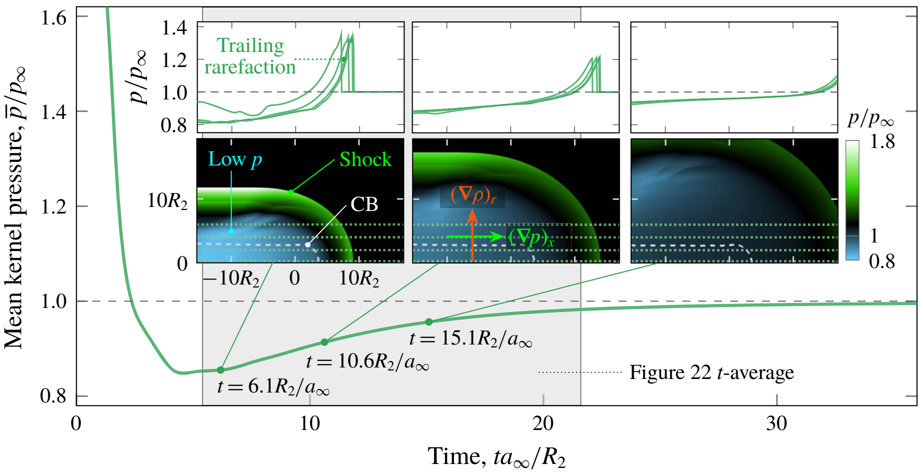

FIGURE 18. Evolution of the mean kernel pressure (3.1) and pressure field, with slices at $r/R_2 = 0$, 2, 4 and 6 showing the x-component of its gradient. Here, $\bar{p}$ is computed by integration over $x \geqslant -9R_2$ only, which corresponds to right half of the $\alpha = 3$, $\beta = 3$ kernel in which $L = 18R_2$.

Because $p_s = p_s(s)$, the s-integration can be recast as

$$\varGamma_s(t) = \frac{\gamma + 1}{4\gamma} \int_{t_b}^{t} \int_{p_{cyl}(\tau)}^{p_{sph}(\tau)} \frac{\rho_s}{\rho_\infty} \left(1 - \frac{\rho_\infty}{\rho_s}\right)^2 \frac{a_\infty^2}{p_\infty} \, \mathrm{d}p_s \, \mathrm{d}\tau, \tag{4.3}$$

where p_{cyl} and p_{sph} are the corresponding cylindrical and spherical shock pressures. The shock formation time t_b is the time at which the compression wave steepens into a shock, as marked by ρ reaching its maximum value, which always occurs on the shock in these simulations. The value of t_b is calculated from the spherical configuration; the cylindrical shock forms only approximately 10 % earlier (figure 15*b*). Conclusions do not depend on this choice since the pre-shock generation of vorticity is small, as seen in the figure 17 inset.

By time $t = t_{sw}$, with $\dot{\varGamma}_s t_{sw} < 0.1\varGamma_s$ signifying the nominal end of significant shock-driven vorticity generation, the shock is too weak to produce even 10 % additional circulation. By this time it is approximately $10R_2$ from the kernel, so it is also unclear that any small addition would couple with the ejection dynamics. The negative circulation remaining after the post-shock cancellation, which removes 72 % of $\varGamma_s$ by t_{sw} (figure 17), will be shown to constitute a relatively small portion of the peak negative circulation, attained as the ambient gas begins to penetrate into the kernel (§ 4.3).

Vorticity generation by the differential blast strength has been connected to vorticity production in other configurations as well (Svetsov *et al.* 1997; Bane *et al.* 2015); for the present case, analysis indicates that a large portion is cancelled by the post-shock rarefaction. We also note that while this idealized spherical–cylindrical geometry facilitates analysis, shock generation of vorticity does not depend on it specifically, only on the increasing shock strength away from the end of the kernel. This key behaviour is supported by experiments, in which measured shock speeds are faster in r than in x (Gregorčič *et al.* 2013), consistent with the observation that the shock evolves from elongated to spherical (Harilal *et al.* 2015; Limbach 2015).

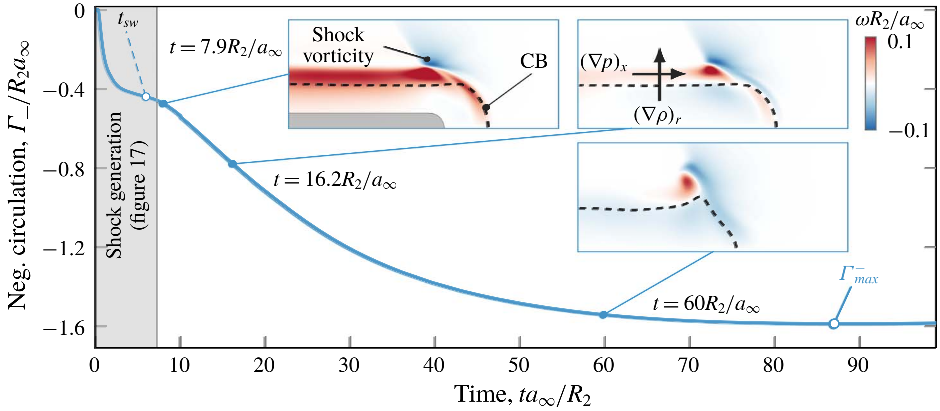

FIGURE 19. Vorticity production near the contact boundary. The short time window of figure 17 covering the period of significant generation by the shock is indicated for reference. The peak negative circulation Γ^-_{max} is attained at $t = 87R_2/a_\infty$.

4.3. *Baroclinic generation at the kernel boundary*

The second mechanism we consider operates over a longer time than the shock, until $t \approx 87R_2/a_\infty = 15t_{sw}$. A low-pressure region around the hot kernel remnant leads to $\boldsymbol{\nabla} p$ that is approximately perpendicular to the strong $\boldsymbol{\nabla} \rho$ associated with the kernel boundary (figure 18). Pressure traces show the important x-component of this gradient and the trailing rarefaction behind the shock. The corresponding evolution of $\Gamma\_$ in figure 19 indicates that this baroclinic torque produces more vorticity than the net left behind the shock. Approximately 28 % of the peak negative circulation Γ^-_{max}, attained at $t = 87R_2/a_\infty$, is produced by the shock before t_{sw}. However, unlike the shock, which deposits vorticity in the dense ambient gas, this mechanism produces vorticity in hot gas with $\rho \lesssim \rho_\infty/5$, so its long-term contribution to the flow is anticipated to be somewhat suppressed. The vorticity from the shock, though deposited at early times, persists and appears unaffected by the baroclinic generation near the contact boundary.

The low-pressure region in figure 18 is due to the expansion following the shock. Figure 20(*a*) depicts Cartesian, cylindrical and spherical analogues, which all produce a shock with a trailing rarefaction shown in figure 20(*b*). In the cylindrical and spherical geometries, this region, including the kernel itself (figure 20*c*), has $p < p_\infty$ before equilibrating, which corresponds to the low pressure in figure 18.

The mechanism by which expansion waves lead to this low pressure is illustrated for the simpler one-dimensional case in figure 21. Figure 21(*a*) shows the pressure and characteristic velocities at $x = 0$. For clarity a sharpened-boundary case $w = R_2/100$ is also shown to better highlight the distinct expansions that progressively decrease the pressure. Each expansion phase corresponds to a rarefaction reaching $x = 0$ (figure 21*b*), with the first originating at the kernel boundary and subsequent rarefactions produced by reflection. Between expansions, the state of the gas at $x = 0$ is constant. Figure 21(*a*) also shows that a kernel with a diffuse boundary, matching our simulations with $w = R_2$, tracks this behaviour though with the overlapping rarefactions smoothing the profiles. Viscous effects are sufficiently weak that increasing Re_{R_2} by a factor of 2 results in less than 1 % change in p and $u \pm a$ in figure 21(*a*).

The same mechanism produces low pressure near the origin in the radial configurations. However, a rarefaction wave propagating towards $r = 0$ must expand

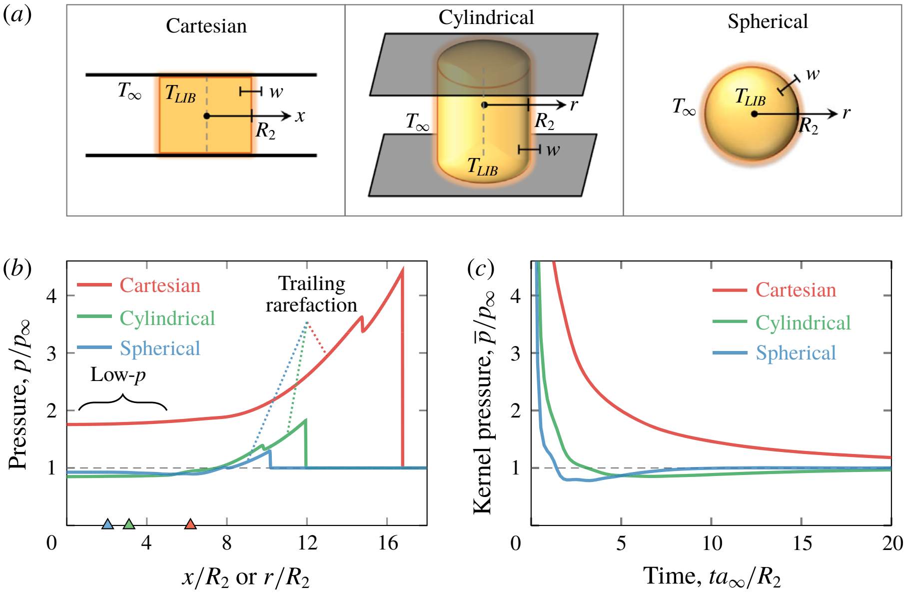

FIGURE 20. (*a*) Analogous one-dimensional configurations produce (*b*) a trailing rarefaction behind the shock and low-pressure region around the kernel, whose (*c*) mean pressure can become sub-ambient. Profiles in (*b*) are shown at $t = 6.3R_2/a_\infty$, with triangle symbols marking the location of the contact boundary.

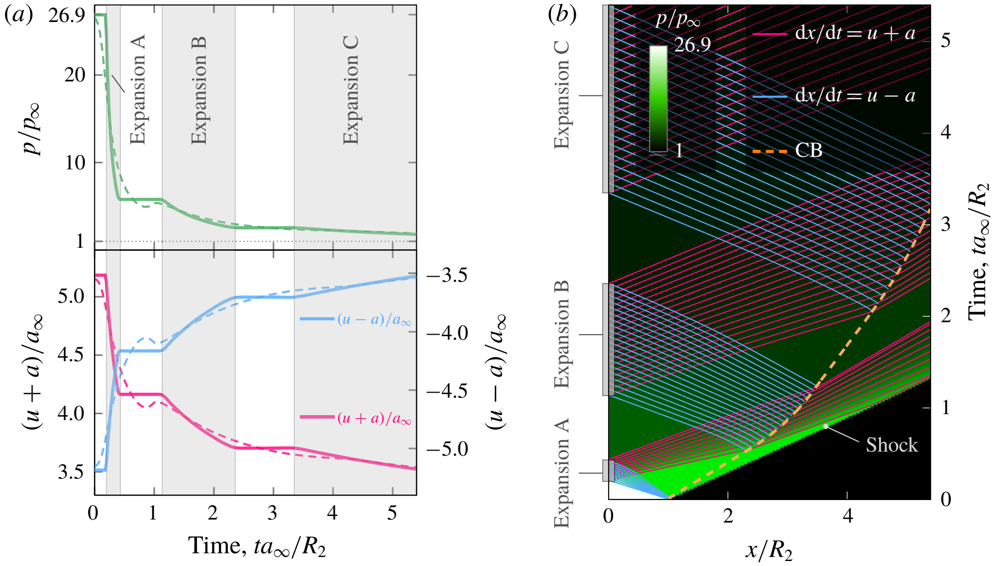

FIGURE 21. (*a*) Evolution of pressure and characteristic velocities at $x = 0$ for the Cartesian configuration, showing a series of expansions that cause the pressure to decrease, both for a sharp boundary (——) $w = R_2/100$ and for the simulated CB scale (–––) $w = R_2$. (*b*) Pressure evolution in x–t ($w = R_2/100$) and subset of characteristics.

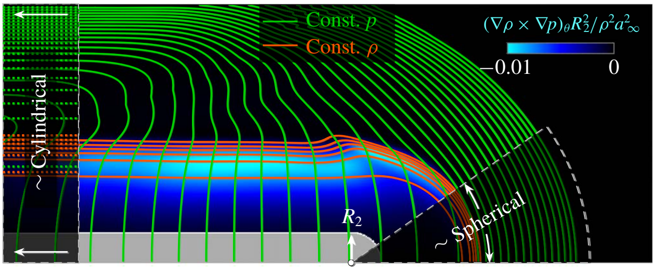

FIGURE 22. Pressure, density and baroclinic torque averaged over $ta_\infty/R_2 \in [5.4, 21.6]$ (indicated in figure 18), with $p/p_\infty \in [0.91, 0.98]$ and $\rho/\rho_\infty \in [0.15, 0.70]$ contour levels. The time interval is chosen to emphasize the trailing rarefaction over early-time shock generation ($t_{sw} = 5.9R_2/a_\infty$); the relative distribution of torque is insensitive to averaging beyond $21.6R_2/a_\infty$. Dotted ($\cdots\cdots$) contour levels show the corresponding one-dimensional cylindrical configuration for reference.

outward-travelling gas into a larger volume than a corresponding wave in a Cartesian geometry (Friedman 1961), resulting in $p < p_\infty$ as noted in figure 20(*b*).

Though direct correspondence to the one-dimensional cases diminishes rapidly in time, a nearly one-dimensional character holds during the expansion in approximately cylindrical and spherical regions, where there is only weak misalignment of $\boldsymbol{\nabla}\rho$ and $\boldsymbol{\nabla}p$ (figure 22). It is interacting rarefactions between these regions that ultimately lead to baroclinic generation in the full model, with nearly perpendicular $\boldsymbol{\nabla}\rho$ and $\boldsymbol{\nabla}p$.

We note that though over-expansion is intrinsic to the radial expansion and has been studied in spherical blasts (Brode 1955; Boyer 1960; Friedman 1961; Ling & Balachandar 2018) and associated with post-breakdown ejections (Spiglanin *et al.* 1995; Morsy & Chung 2002), the resulting $\bar{p} < p_\infty$ is not necessary for vorticity generation. The mechanism requires only that rarefactions behind the shock, which decrease the kernel pressure by reflection at $r = 0$, produce a misaligned pressure gradient across the kernel boundary.

4.4. *Dependence on* T_{LIB}/T_∞

Shock generation is confirmed to be the increasingly weaker mechanism for increasing T_{LIB}/T_∞ in figure 23. The shock-generated negative circulation $\Gamma_{sw}^- \equiv \Gamma_-(t_{sw})$ is consistently smaller than the peak Γ_{max}^-, with the shock's relative contribution decreasing with higher T_{LIB}. Baroclinic generation in the trailing rarefaction is thus anticipated to be the dominant mechanism for most cases of interest.

4.5. *Dependence on* R_2

With R_2 the only length scale, it is straightforward to assess viscous effects in this configuration. Focusing on the circulation,

$$\frac{\Gamma}{R_2 a_\infty} = f\left(\frac{ta_\infty}{R_2}, Re_{R_2}, \frac{T_{LIB}}{T_\infty}, \gamma, Pr\right),$$

figure 24 shows that $\Gamma/R_2 a_\infty$ and $\Gamma_-/R_2 a_\infty$ are Re_{R_2}-independent for $Re_{R_2} \gtrsim 2000$, implying

$$\Gamma = R_2 a_\infty f\left(\frac{T_{LIB}}{T_\infty}\right) \tag{4.4}$$

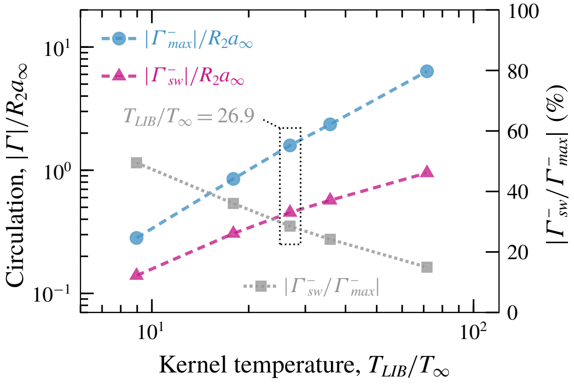

FIGURE 23. Dependence of the peak negative circulation Γ^-_{max} and shock-generated $\Gamma^-_{sw} \equiv \Gamma_-(t_{sw})$ on T_{LIB}/T_∞. For the most intense case, meshes with four times finer spacing than those in table 1 were required to establish mesh independence.

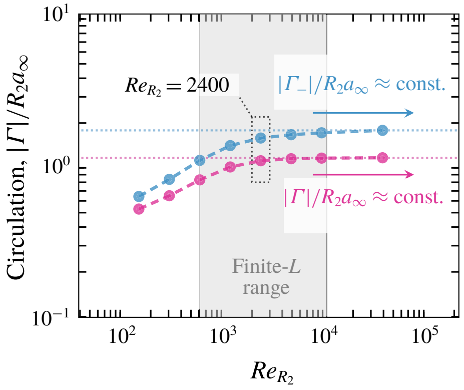

FIGURE 24. Dependence of $|\Gamma|$ and $|\Gamma_-|$ on Re_{R_2} in the semi-infinite configuration at $t = 100R_2/a_\infty$, by which time Γ is only slowly varying. The analysis in §§ 4.2 and 4.3 is conducted at $Re_{R_2} = 2400$; the slight slope in $|\Gamma_-|$ for $Re_{R_2} > 2400$ corresponds to only 10 % change over one decade. The range of Re_{R_1} and Re_{R_2} corresponding to the finite-L cases in § 5 is shown here for reference.

at a fixed ta_∞/R_2 and constant γ and Pr. Thus for $Re_{R_2} \gtrsim 2000$, larger R_2 leads to proportionally greater circulation, which will inform the finite-L kernel discussion for high aspect ratios α in § 5.

5. Vorticity generation for finite L

Shock generation of vorticity occurs at each end of the finite-L kernel by the same mechanism as in the semi-infinite configuration (§ 4.2). However, because it derives from a relatively short-lived pressure gradient along the shock front (e.g. $t_{sw} = 0.33L/a_\infty$ for R_2 with $\alpha = 3$, $\beta = 3$), which quickly separates from the kernel, we do not anticipate, nor have we observed, that it is qualitatively changed by disturbances from the other end. As will be shown, the kernel asymmetry primarily affects baroclinic generation along the contact boundary, which appears to leave shock

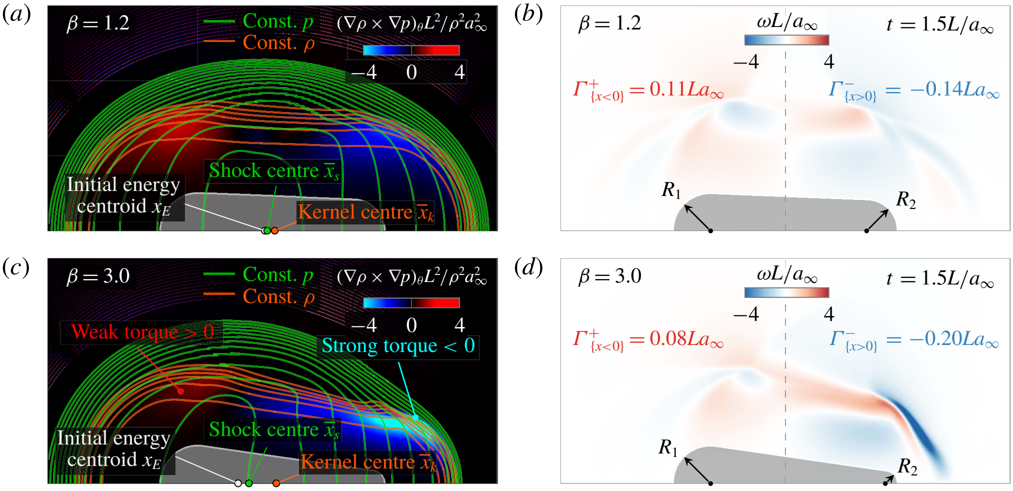

FIGURE 25. Pressure, density and baroclinic torque averaged over $ta_\infty/L \in [0.3, 1.5]$, with $p/p_\infty \in [0.84, 0.94]$ and $\rho/\rho_\infty \in [0.15, 0.70]$ contour levels, and instantaneous vorticity field for (*a*,*b*) $\beta = 1.2$ and (*c*,*d*) $\beta = 3.0$, both with $\alpha = 3$. The time interval is chosen to emphasize the trailing rarefaction over early-time shock generation; the relative distribution of torque is insensitive to averaging beyond $1.5L/a_\infty$. The shock and kernel centres (*t*-averages $\bar{x}_s$ and $\bar{x}_k$ shown) are the midpoints of their respective *x*-extents at $r = 0$; their offset varies by $0.05L$ over the time interval. The initial energy centroid is $\int x\rho_\infty(e - e_\infty)\,\mathrm{d}V / \int \rho_\infty(e - e_\infty)\,\mathrm{d}V$. Positive and negative circulation in $x < 0$ and $x > 0$, respectively, as marked in (*b*) and (*d*).

vorticity outside the boundary unaffected (as seen in figure 19). Furthermore, based on the semi-infinite cases shown in figure 23, shock generation is expected to be the weaker mechanism for finite-L kernels as well.

We therefore focus on generation by the trailing rarefaction, which is significantly affected by kernel asymmetry. Figure 25(*a*,*c*) shows that increasing β leads to increased negative torque at the smaller R_2 end, which is consistent with the greater negative circulation $\Gamma^-_{\{x>0\}}$ on the R_2 side at $t = 1.5L/a_\infty$ shown in figure 25(*b*,*d*). Relative to the kernel centre, the centrepoint of the shock (and consequently its rarefaction) is biased towards the larger R_1 side, where more energy is deposited, leaving it misaligned with the kernel centre, as suggested by Bradley *et al.* (2004). This *x*-offset between the apparent shock centre and kernel is greater for the more asymmetric $\beta = 3$ kernel and augments $\boldsymbol{\nabla} p \times \boldsymbol{\nabla} \rho$ near the smaller end. For the $\alpha = 3$, $\beta = 3$ case, as an example, this leads to $\Gamma < 0$ (see figure 10).

Figure 26 shows this effect more broadly: at each α, a larger energy centroid offset $|x_E|$, corresponding to a more asymmetric kernel, consistently produces a larger shock–kernel offset (figure 26*a*), which is associated with greater negative circulation on the R_2 side (figure 26*b*). The non-dimensionalization $\Gamma^-_{\{x>0\}}/R_2 a_\infty$ removes the increase in $\Gamma^-_{\{x>0\}}$ due solely to larger R_2, as shown in the semi-infinite configuration (figure 24). With the $\alpha = 12$ cases having $Re_{R_2} \in [600, 1200]$, this smaller-end intensification appears to persist even for the low-Re_{R_2} cases.

This offset effect increases $\Gamma^-_{\{x>0\}}$ for all $\beta > 1$ but is countered by a competing effect for $\alpha \geqslant 5$ that leads to the transition in the relative circulation produced at either end, seen in figure 27. For larger α, the shock–kernel offset is relatively small,

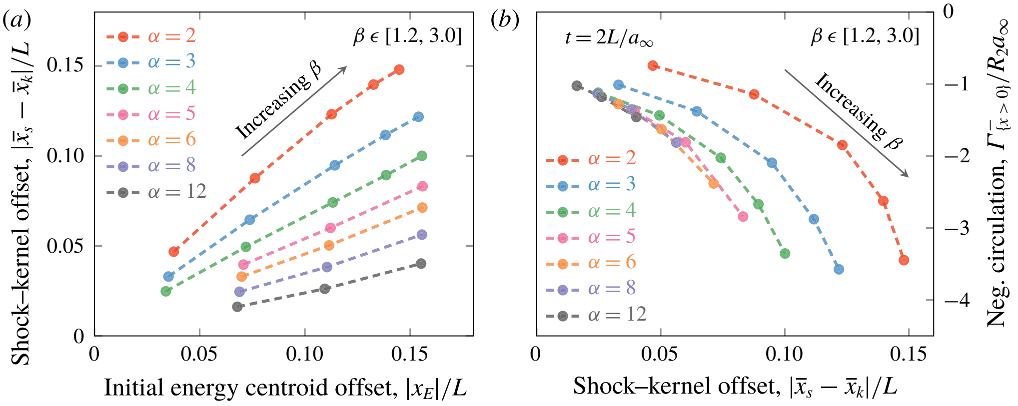

FIGURE 26. (a) Larger $x_E \equiv \int x\rho_\infty(e-e_\infty)\,\mathrm{d}V/\int \rho_\infty(e-e_\infty)\,\mathrm{d}V$ leads to a greater shock–kernel offset and (b) stronger $\Gamma^-_{\{x>0\}}$ at $t = 2L/a_\infty$, by which time Γ is approximately constant for all cases. The shock and kernel centres ($\bar{x}_s$ and $\bar{x}_k$ respectively) are averaged over $t \in [0.3, 2]L/a_\infty$ to emphasize generation by the trailing rarefaction over early-time shock generation.

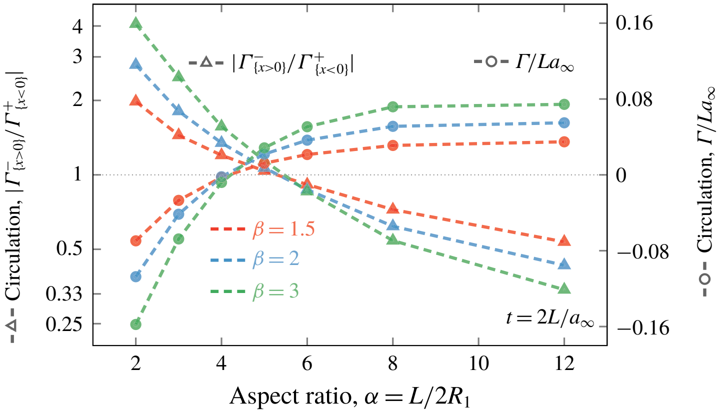

FIGURE 27. Dependence of the net circulation and circulation ratio on α at $t = 2L/a_\infty$.

and the associated increase in negative circulation weak (figure 26b). Though finite-L effects hamper direct comparison, the dynamics of each end of an elongated kernel more closely resembles that of the semi-infinite configuration, in which smaller R_2 produce less circulation (figure 24). Thus the sign change of Γ results from the positive vorticity of the larger R_1 end simply overwhelming the negative vorticity of the R_2 end. For sufficiently large α the effect is compounded by viscosity further decreasing the circulation at the R_2 end.

A secondary effect also contributes to this transition. During the early-time expansion (figure 28a), a tangential pressure gradient develops along the conical region of the CB because gas at smaller r depressurizes faster than that at larger r. Dimensional considerations of the corresponding one-dimensional configuration suggest $p/p_\infty = g(ta_\infty/R_0)$, which is confirmed in figure 28(b) for $\alpha = 8$. The resulting ∇p and $\nabla \rho$ misalignment produces positive vorticity in all finite-L cases,

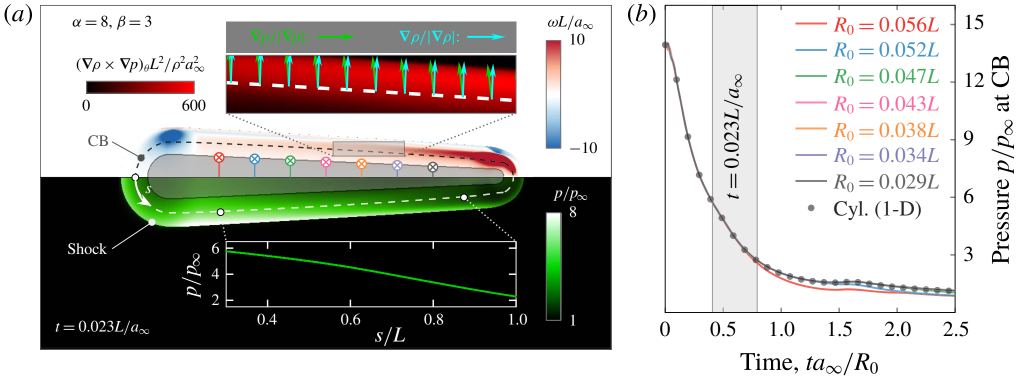

FIGURE 28. (*a*) Vorticity and pressure at $t = 0.023L/a_\infty$ for $\alpha = 8$, $\beta = 3$ showing positive baroclinic generation along the conical section of the CB due to the tangential pressure variation $p(s)$. (*b*) Pressure traces at the CB, extracted at $x/L = \{-0.3, -0.2, \ldots, 0.3\}$, match the corresponding cylindrically symmetric case for the early times shown. The initial CB location $r = R_0$ at each x is marked by $\otimes$ in (*a*).

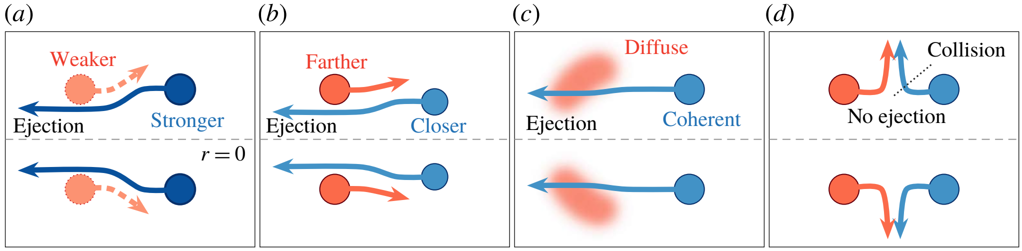

FIGURE 29. Four basic modes of vorticity interaction can lead either to ejection – by mismatched (*a*) strength, (*b*) radial location or (*c*) formation time – or (*d*) to its failure. We note that although (*d*) could be considered as radially ‘ejecting’ and resembles flow produced by electrode sparks (e.g. Kono *et al.* 1988; Bane *et al.* 2015), it is does not correspond to the axial ejection being analysed.

becoming relatively more important for larger α, with its longer kernel and smaller ends. As will be shown in § 6, the $\alpha \approx 5$ transition to $\Gamma > 0$ (figure 27) is important for subsequent ejection characteristics.

6. Ejection and its reversal

As seen in § 3.2, for ejection to occur a vortex-ring-like structure must separate from the rest of the evolving hydrodynamics. We anticipate means by which this could occur in § 6.1. With this context, the mechanisms leading to the ejection characteristics seen in figure 11 are then described in §§ 6.2 and 6.3.

6.1. *Candidate end–end vorticity interactions*

It is clear from analysis of the semi-infinite configuration (§ 4) that vorticity generated at either end of the kernel auto-advects towards its centre. Several candidate scenarios for their subsequent interaction, shown schematically in figure 29, describe how an ejection can form or not. In figure 29(*a*), ejection occurs due to a vortex-ring-like structure simply being stronger at one end of the kernel than the other. Another route to ejection could result from a size mismatch. If the ring-like structure on one end is significantly smaller, as shown in figure 29(*b*), it could then auto-advect through the centre of the larger structure, propagating at a higher velocity because of its smaller radius. In both of these cases, the opposing ring-like structure is pushed outward and slows as the ejecting structure is compressed inward and accelerates, leading to its prominent ejection. The experimental visualization in figure 1(*a*) seems to be such an example. While these first two scenarios presume that coherent vortical structures have formed prior to interaction, the third scenario in figure 29(*c*) concerns their time to form, which can depend on both the strength and radial location of distributed vorticity. The vorticity at one end may collect into a structure too slowly to collectively interact with the vorticity from the other end, which then ejects. Though the remaining vorticity may form into a ring subsequently, we anticipate that it would be significantly disrupted by and occur after the passing of the ejection and be pushed to larger r. Finally, in figure 29(*d*), we anticipate the primary means by which we expect ejection to fail: if the vorticity forms into similar structures at the ends of the kernel concurrently, vortex-ring dynamics suggests that the structures will collide and progress outwards as a vortex pair that decelerates. Vorticity diffusion is neglected in this discussion: with $\rho = \rho_\infty/10$ and $\mu = \mu_\infty$, a characteristic time τ to diffuse over $l = L/2$,

$$\tau = \frac{1}{\pi^2}\frac{l^2}{\mu/\rho} = \frac{Re}{40\pi^2}\frac{L}{a_\infty},$$

is much slower ($\tau \approx 110L/a_\infty$ for most cases) than the typical times observed ($\sim 10L/a_\infty$) to form an ejecting vortex ring (for example in figure 9*c*–*d*).

Clearly these are idealizations of a complicated flow, and there is no expectation of a precise decomposition into such a clean a set of processes. However, as we analyse the evolution of the simulated flows in the following sections, we will see all these for different configurations. Moreover, these hydrodynamic scenarios are not limited by the specific breakdown model considered here, as a more complicated geometry or non-uniform kernel temperature, for example, will also lead to such asymmetries in the vorticity interaction.

6.2. *Ejection failure with decreasing β*

As the kernel changes from near symmetry ($1/1.2 \lesssim \beta \lesssim 1.2$) to greater asymmetry ($\beta \gtrsim 1.5$ or $\beta \lesssim 1/1.5$), we see in figure 30 the anticipated transition from the collision mechanism (figure 29*d*) to an ejection mechanism (figure 29*b*). We focus specifically on the vorticity at the ends of the kernel as marked. While the peak value does not necessarily occur there, we anticipate that the interaction of this end vorticity, with its dense gas and inward-pointing momentum, will primarily determine the character of the ejection.

In figure 30(*d*,*e*), the positive and negative vorticity produced at the ends of the $\beta = 1.2$ kernel have almost mirrored trajectories as they collect into coherent vortex structures. Due to their similar strength and radii, they collide at the $x = 0$ symmetry plane, after which the most prominent structure radiates outward (figure 30*f*). Without the axisymmetric constraint, azimuthal instabilities would presumably cause this to break into the more irregular features seen in experiments (figure 2*g*), though agreement with experiment (e.g. figure 6*a*,*b*) is still achieved during the earlier phase of more organized flow. With modestly larger asymmetry ($\beta = 1.5$), the negative

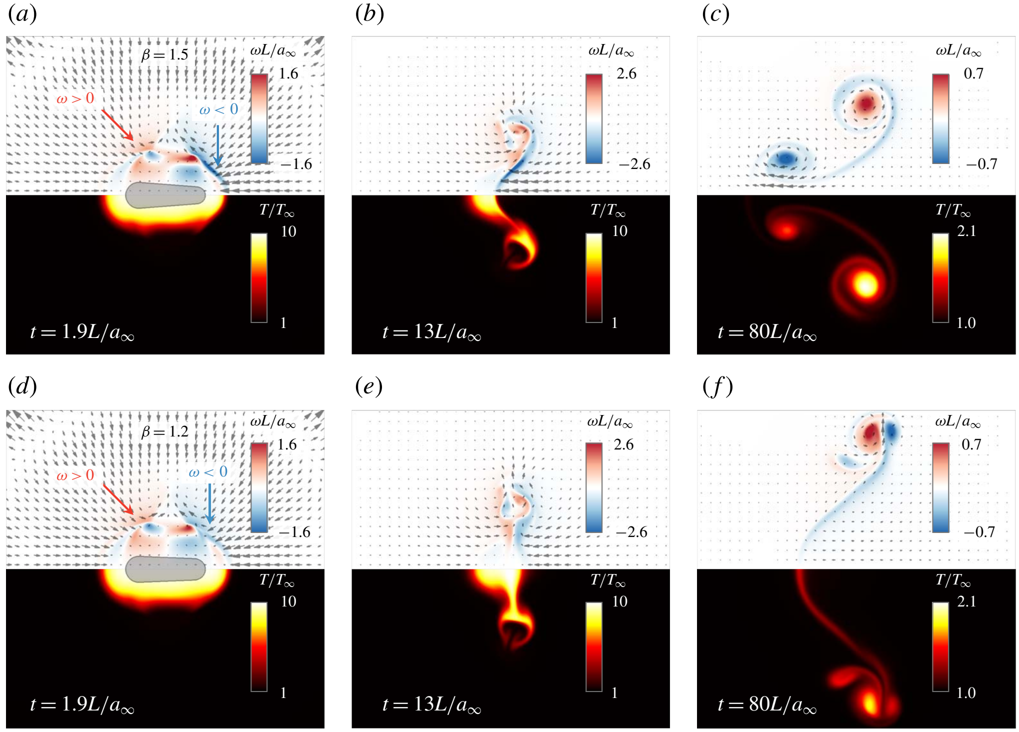

FIGURE 30. A $\beta = 1.5$, $R_2 = 0.11L$ kernel (*a–c*) forms a left-propagating vortex ring, whereas a $\beta = 1.2$, $R_2 = 0.14L$ kernel (*d–f*) does not. The initial kernels are shown in grey, both with $\alpha = 3$, and vectors correspond to $\rho \boldsymbol{u}$.

vorticity from the smaller end of the kernel collects sufficiently close to $r = 0$ that it passes through the opposing positive vorticity, which subsequently collects into a larger ring (figure 30*a–c*).

The other two ejection mechanisms (figure 29*a*,*c*) also play a role. Early, at $t = 1.9L/a_\infty$, the vorticity is similarly distributed for both the $\beta = 1.2$ and $\beta = 1.5$ kernels, but the latter has more concentrated negative vorticity near the smaller end, which results from the shock–kernel offset as discussed in § 5. By $t = 13L/a_\infty$ (figure 30*b*), though not yet formed into a distinct ring, its relative coherency suggests the figure 29(*c*) scenario. Its greater strength also facilitates passage through the opposing structure, similar to figure 29(*a*), and later constitutes the ejection.

To further understand this transition between collision and ejection, we revisit the semi-infinite configuration and take t_p to be the time the vorticity penetrates the kernel,

$$\xi(x = -R_2, r = 0, t = t_p) = 0,$$

where ξ is the advected scalar (2.2) and $x = 0$ is labelled in figure 12. This marks the time at which the contact boundary (2.3) intersects the initial centrepoint of the hemispherical cap, occurring between figures 13(*b*) and 13(*c*) for example. Following the same arguments leading to (4.4), we anticipate the penetration time and the

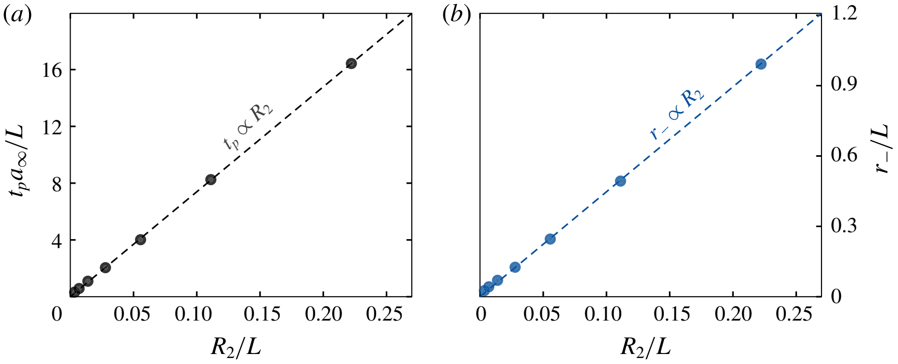

FIGURE 31. Essentially linear relationship of (*a*) penetration time t_p and (*b*) position of negative vorticity r_- (6.1) at t_p with respect to the cap radius R_2 in the semi-infinite configuration.

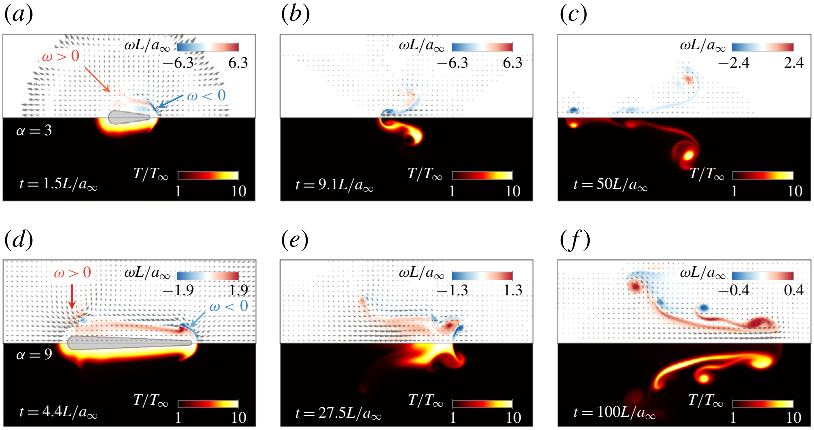

FIGURE 32. The $\alpha = 3$, length-L kernel (*a–c*) produces a leftward ejection, whereas the $\alpha = 9$, length-$3L$ kernel (*d–f*) produces a rightward ejection. Initial kernels are shown in grey, both with $\beta = 3$, and vectors correspond to $\rho \boldsymbol{u}$.

negative vorticity position,

$$r_- \equiv \frac{\displaystyle\iint_{\omega<0} \omega r \,\mathrm{d}x\,\mathrm{d}r}{\displaystyle\iint_{\omega<0} \omega \,\mathrm{d}x\,\mathrm{d}r}, \tag{6.1}$$

to be proportional to R_2 as well – $t_p \propto R_2$ and $r_- \propto R_2$ – which is remarkably accurate (figure 31). The smaller end of the finite-L kernel, therefore, produces vorticity closer to $r = 0$ and thus penetrates earlier and passes through that of the opposite end.

Of course, given the complexity of the flow, additional factors are expected to affect whether collision occurs. The collision model is predicated on vorticity forming into coherent structures before their critical interaction, but the figure 29(*c*) formation-time mechanism can interrupt this process at the larger end and partially account for the weak resistance encountered by the negative vorticity in figure 30(*b*). While it is difficult to determine the relative importance of strength, location, and timing – the three ejection mechanisms of figure 29(*a*–*c*) – from these observations alone, the outcome is clear: the vorticity from the smaller end is more intense and stays close to the axis in a fast-moving ring that ejects.

6.3. *Reversal with increasing α*

Ejection reversal for $\beta \lessgtr 1$ is obvious due to symmetry. However, kernel length (α) can also lead to reversal as seen in figure 11. Figure 32 compares $\alpha = 3$ to $\alpha = 9$. Figure 32(*a*–*b*) for $\alpha = 3$ seems to reflect the figure 29(*c*) mechanism: the concentrated negative vorticity penetrates the kernel and passes through the still diffuse positive vorticity. In contrast, the longer $\alpha = 9$ kernel allows structures to form and penetrate at both ends (figure 32*d*–*e*). The smaller-end vorticity appears more concentrated but is weaker, for reasons discussed in § 5, and is subsequently overwhelmed by strong positive vorticity in a reversal of the figure 29(*a*) strength mismatch mechanism. The result is a change in the ejection direction (figure 32*c*,*f*). Thus, if the kernel is long enough, t_p for both ends is earlier than their time of interaction, and ejection depends primarily on relative strengths. For this case, the relative position and coherency of vorticity (figure 29*b*,*c*) appear to be secondary to this strength asymmetry. As anticipated at $t = 2L/a_\infty$ in figure 27, this reversal with respect to α indeed corresponds to a change in the sign of $\varGamma$.

7. Conclusion

Although it is a simplification of complex early-time plasma dynamics, the ideal-gas hot-spot model reproduces key features observed in the flow created by laser-induced breakdowns, particularly the ejection of hot fluid and how subtle changes in the kernel cause this to change. The assumption of axisymmetry, though obviously a model in the late stages of ejection propagation, provides agreement with velocimetry measurements of the earlier, critical vorticity dynamics and makes the detailed mapping of the hydrodynamic response to geometry parameters computationally accessible. These simulations show that the ejections, when they occur, have a vortex-ring-like character and are formed by two important vorticity-generating mechanisms: tangential variations in the shock strength, and baroclinic generation in the trailing rarefaction, with the latter being the more important mechanism for the conditions studied. Ejection occurs if there is sufficient mismatch in the strength, radial position or formation time of vorticity produced at either end of the kernel, which we show can be pronounced for even mildly asymmetric geometries. In such cases, the smaller end produces vorticity that, due to its intensity and proximity to the $r = 0$ axis, rapidly penetrates the kernel and passes through vorticity of the opposite end. This process is forestalled for near-symmetric kernels, in which case the vortical structures collide and no ejection occurs. Obvious fore–aft asymmetry effects ($\beta > 1$ and $\beta < 1$) lead to a change in direction, but more surprisingly so does kernel aspect ratio (α). For shorter kernels, asymmetry intensifies torque at the smaller end and leads to ejection. For sufficiently long kernels, however, the vortex rings fully form at either end before interacting, in which case the larger end overwhelms the smaller, and the ejection reverses. The close connection between the kernel geometry and ejection characteristics analysed here offers opportunities to further tailor the ejection.

Acknowledgements

This material is based in part upon work supported by the Department of Energy, National Nuclear Security Administration, under award no. DE-NA0002374. The authors gratefully acknowledge M. D. Koll, J. E. Retter and G. S. Elliott for providing invaluable experimental data.

REFERENCES

ADELGREN, R., ELLIOT, G., KNIGHT, D., ZHELTOVODOV, A. & BEUTNER, T. 2001 Energy deposition in supersonic flows. In *39th Aerospace Sciences Meeting and Exhibit*, pp. 885–917. American Institute of Aeronautics & Astronautics (AIAA).

ADELGREN, R. G., YAN, H., ELLIOTT, G. S., KNIGHT, D. D., BEUTNER, T. J. & ZHELTOVODOV, A. A. 2005 Control of Edney IV interaction by pulsed laser energy deposition. *AIAA J.* **43** (2), 256–269.

ALBERTI, A., MUNAFÒ, A., KOLL, M. D., NISHIHARA, M., PANTANO, C., FREUND, J. B., ELLIOTT, G. S. & PANESI, M. 2019 Laser-induced non-equilibrium plasma kernel dynamics. *J. Phys.* D. **53** (2), 025201.

ARCHER, P. J., THOMAS, T. G. & COLEMAN, G. N. 2008 Direct numerical simulation of vortex ring evolution from the laminar to the early turbulent regime. *J. Fluid Mech.* **598**, 201–226.

BANE, S. P. M., ZIEGLER, J. L. & SHEPHERD, J. E. 2015 Investigation of the effect of electrode geometry on spark ignition. *Combust. Flame* **162** (2), 462–469.

BLAKE, J. R. & GIBSON, D. C. 1987 Cavitation bubbles near boundaries. *Annu. Rev. Fluid Mech.* **19** (1), 99–123.

BOGEY, C., DE CACQUERAY, N. & BAILLY, C. 2009 A shock-capturing methodology based on adaptative spatial filtering for high-order non-linear computations. *J. Comput. Phys.* **228** (5), 1447–1465.

BOYER, D. W. 1960 An experimental study of the explosion generated by a pressurized sphere. *J. Fluid Mech.* **9** (3), 401–429.

BRADLEY, D., SHEPPARD, C. G. W., SUARDJAJA, I. M. & WOOLLEY, R. 2004 Fundamentals of high-energy spark ignition with lasers. *Combust. Flame* **138** (1–2), 55–77.

BRIESCHENK, S., O'BYRNE, S. & KLEINE, H. 2013*a* Laser-induced plasma ignition studies in a model scramjet engine. *Combust. Flame* **160** (1), 145–148.

BRIESCHENK, S., O'BYRNE, S. & KLEINE, H. 2013*b* Visualization of jet development in laser-induced plasmas. *Opt. Lett.* **38** (5), 664–666.

BRODE, H. L. 1955 Numerical solutions of spherical blast waves. *J. Appl. Phys.* **26** (6), 766–775.

COLONIUS, T. 2004 Modeling artificial boundary conditions for compressible flow. *Annu. Rev. Fluid Mech.* **36**, 315–345.

DUMITRACHE, C., VANOSDOL, R., LIMBACH, C. M. & YALIN, A. P. 2017 Control of early flame kernel growth by multi-wavelength laser pulses for enhanced ignition. *Sci. Rep.* **7** (1), 10239.

FREUND, J. B. 1997 Proposed inflow/outflow boundary condition for direct computation of aerodynamic sound. *AIAA J.* **35** (4), 740–742.

FRIEDMAN, M. P. 1961 A simplified analysis of spherical and cylindrical blast waves. *J. Fluid Mech.* **11** (1), 1–15.

GHOSH, S. & MAHESH, K. 2008 Numerical simulation of the fluid dynamic effects of laser energy deposition in air. *J. Fluid Mech.* **605**, 329–354.

GIBBONS, N., GEHRE, R., BRIESCHENK, S. & WHEATLEY, V. 2018 Blast wave-induced mixing in a laser ignited hypersonic flow. *J. Fluids Engng* **140** (5), 050902.

GLUMAC, N. G. & ELLIOTT, G. S. 2007 The effect of ambient pressure on laser-induced plasmas in air. *Opt. Lasers Engng* **45** (1), 27–35.

GLUMAC, N. G., ELLIOTT, G. S. & BOGUSZKO, M. 2005 Temporal and spatial evolution of a laser spark in air. *AIAA J.* **43** (9), 1984–1994.

GREGORČIČ, P., DIACI, J. & MOŽINA, J. 2013 Two-dimensional measurements of laser-induced breakdown in air by high-speed two-frame shadowgraphy. *Appl. Phys.* A **112** (1), 49–55.

Harilal, S. S., Brumfield, B. E. & Phillips, M. C. 2015 Lifecycle of laser-produced air sparks. *Phys. Plasmas* **22** (6), 063301.

Harilal, S. S., Miloshevsky, G. V., Diwakar, P. K., LaHaye, N. L. & Hassanein, A. 2012 Experimental and computational study of complex shockwave dynamics in laser ablation plumes in argon atmosphere. *Phys. Plasmas* **19** (8), 083504.

Hayes, W. D. 1957 The vorticity jump across a gasdynamic discontinuity. *J. Fluid Mech.* **2** (6), 595–600.

Johnsen, E., Larsson, J., Bhagatwala, A. V., Cabot, W. H., Moin, P., Olson, B. J., Rawat, P. S., Shankar, S. K., Sjögreen, B., Yee, H. C. *et al.* 2010 Assessment of high-resolution methods for numerical simulations of compressible turbulence with shock waves. *J. Comput. Phys.* **229** (4), 1213–1237.

Kandala, R. & Candler, G. V. 2004 Numerical studies of laser-induced energy deposition for supersonic flow control. *AIAA J.* **42** (11), 2266–2275.

Koll, M. D., Elliott, G. S. & Freund, J. B. 2020 Particle image velocimetry of a nano-second laser induced breakdown in air. In *AIAA Scitech 2020 Forum*, pp. 2047–2058.

Kono, M., Niu, K., Tsukamoto, T. & Ujiie, Y. 1988 Mechanism of flame kernel formation produced by short duration sparks. In *Symposium (International) on Combustion*, pp. 1643–1649. Elsevier.

Lacaze, G., Cuenot, B., Poinsot, T. & Oschwald, M. 2009 Large eddy simulation of laser ignition and compressible reacting flow in a rocket-like configuration. *Combust. Flame* **156** (6), 1166–1180.

Lele, S. K. 1992 Compact finite difference schemes with spectral-like resolution. *J. Comput. Phys.* **103** (1), 16–42.

Lighthill, M. J. 1957 Dynamics of a dissociating gas. Part I. Equilibrium flow. *J. Fluid Mech.* **2** (1), 1–32.

Limbach, C. M. 2015 Characterization of nanosecond, femtosecond and dual pulse laser energy deposition in air for flow control and diagnostic applications. PhD thesis, Princeton University, Princeton, NJ.

Ling, Y. & Balachandar, S. 2018 Asymptotic scaling laws and semi-similarity solutions for a finite-source spherical blast wave. *J. Fluid Mech.* **850**, 674–707.

Liu, J. & Wang, W. 2009 Characterization and regularity for axisymmetric solenoidal vector fields with application to Navier–Stokes equation. *SIAM J. Math. Anal.* **41** (5), 1825–1850.

Lo, S.-C., Blaisdell, G. A. & Lyrintzis, A. S. 2010 High-order shock capturing schemes for turbulence calculations. *Intl J. Numer. Meth. Fluids* **62** (5), 473–498.

Massa, L. L. & Freund, J. B. 2016 An integrated predictive simulation model for the plasma-assisted ignition of a fuel jet in a turbulent crossflow. In *54th AIAA Aerospace Sciences Meeting*, pp. 2154–2201. American Institute of Aeronautics & Astronautics (AIAA).

Massa, L. L. & Freund, J. B. 2017 Plasma-combustion coupling in a dielectric-barrier discharge actuated fuel jet. *Combust. Flame* **184**, 208–232.

Meyerand, R. G. & Haught, A. F. 1963 Gas breakdown at optical frequencies. *Phys. Rev. Lett.* **11** (9), 401–403.

Morgan, C. G. 1975 Laser-induced breakdown of gases. *Rep. Prog. Phys.* **38** (5), 621–665.

Morsy, M. H. & Chung, S. H. 2002 Numerical simulation of front lobe formation in laser-induced spark ignition of CH_4/air mixtures. *Proc. Combust. Inst.* **29** (2), 1613–1619.

Nishihara, M., Freund, J. B., Glumac, N. G. & Elliott, G. S. 2018 Influence of mode-beating pulse on laser-induced plasma. *J. Phys.* D **51** (13), 135601.

Phuoc, T. X. 2006 Laser-induced spark ignition fundamental and applications. *Opt. Lasers Engng* **44** (5), 351–397.

Picone, J. M. & Boris, J. P. 1983 Vorticity generation by asymmetric energy deposition in a gaseous medium. *Phys. Fluids* **26** (2), 365–382.

Picone, J. M. & Boris, J. P. 1988 Vorticity generation by shock propagation through bubbles in a gas. *J. Fluid Mech.* **189**, 23–51.

Pirozzoli, S. 2002 Conservative hybrid compact-WENO schemes for shock–turbulence interaction. *J. Comput. Phys.* **178** (1), 81–117.

PLESSET, M. S. & MITCHELL, T. P. 1956 On the stability of the spherical shape of a vapor cavity in a liquid. *Q. Appl. Maths* **13** (4), 419–430.

POINSOT, T. J. & LELE, S. K. 1992 Boundary conditions for direct simulations of compressible viscous flows. *J. Comput. Phys.* **101** (1), 104–129.

RANJAN, D., NIEDERHAUS, J., MOTL, B., ANDERSON, M., OAKLEY, J. & BONAZZA, R. 2007 Experimental investigation of primary and secondary features in high-Mach-number shock–bubble interaction. *Phys. Rev. Lett.* **98** (2), 024502.

RETTER, J. E., GLUMAC, N. G. & ELLIOTT, G. S. 2017 XPACC: stand burner ignition profiles. *Tech. Rep.* University of Illinois at Urbana-Champaign, IL.

RIGGINS, D., NELSON, H. F. & JOHNSON, E. 1999 Blunt-body wave drag reduction using focused energy deposition. *AIAA J.* **37** (4), 460–467.

RONNEY, P. D. 1994 Laser versus conventional ignition of flames. *Opt. Engng* **33** (2), 510–522.

SCHMIEDER, R. W. 1981 Laser spark ignition and extinction of a methane–air diffusion flame. *J. Appl. Phys.* **52** (4), 3000–3003.

SPIGLANIN, T. A., MCILROY, A., FOURNIER, E. W., COHEN, R. B. & SYAGE, J. A. 1995 Time-resolved imaging of flame kernels: laser spark ignition of $H_2/O_2/Ar$ mixtures. *Combust. Flame* **102** (3), 310–328.

SVETSOV, V., POPOVA, M., RYBAKOV, V., ARTEMIEV, V. & MEDVEDUK, S. 1997 Jet and vortex flow induced by anisotropic blast wave: experimental and computational study. *Shock Waves* **7** (6), 325–334.

THIELE, M., WARNATZ, J. & MAAS, U. 2000 Geometrical study of spark ignition in two dimensions. *Combust. Theor. Model.* **4** (4), 413–434.

THOMPSON, K. W. 1990 Time-dependent boundary conditions for hyperbolic systems, II. *J. Comput. Phys.* **89** (2), 439–461.

THOMPSON, P. A. 1971 *Compressible-fluid Dynamic*. McGraw-Hill.

TORIKAI, H., SOGA, Y. & ITO, A. 2017 Schlieren visualization of blast extinguishment with laser-induced breakdown. *Proc. Combust. Inst.* **36** (2), 3297–3304.

TRUESDELL, C. 1952 On curved shocks in steady plane flow of an ideal fluid. *J. Aero. Sci.* **19** (12), 826–828.